Biophysical*Journal*
Article

Biophysical Society

New Continuum Approaches for Determining Protein-Induced Membrane Deformations

David Argudo,[1] Neville P. Bethel,[1] Frank V. Marcoline,[1] Charles W. Wolgemuth,[2] and Michael Grabe[1,*]
[1]Cardiovascular Research Institute, Department of Pharmaceutical Chemistry, University of California San Francisco, San Francisco, California and [2]Departments of Molecular and Cellular Biology and Physics, University of Arizona, Tucson, Arizona

ABSTRACT The influence of the membrane on transmembrane proteins is central to a number of biological phenomena, notably the gating of stretch activated ion channels. Conversely, membrane proteins can influence the bilayer, leading to the stabilization of particular membrane shapes, topological changes that occur during vesicle fission and fusion, and shape-dependent protein aggregation. Continuum elastic models of the membrane have been widely used to study protein-membrane interactions. These mathematical approaches produce physically interpretable membrane shapes, energy estimates for the cost of deformation, and a snapshot of the equilibrium configuration. Moreover, elastic models are much less computationally demanding than fully atomistic and coarse-grained simulation methodologies; however, it has been argued that continuum models cannot reproduce the distortions observed in fully atomistic molecular dynamics simulations. We suggest that this failure can be overcome by using chemically and geometrically accurate representations of the protein. Here, we present a fast and reliable hybrid continuum-atomistic model that couples the protein to the membrane. We show that the model is in excellent agreement with fully atomistic simulations of the ion channel gramicidin embedded in a POPC membrane. Our continuum calculations not only reproduce the membrane distortions produced by the channel but also accurately determine the channel's orientation. Finally, we use our method to investigate the role of membrane bending around the charged voltage sensors of the transient receptor potential cation channel TRPV1. We find that membrane deformation significantly stabilizes the energy of insertion of TRPV1 by exposing charged residues on the S4 segment to solution.

INTRODUCTION

During the past decade there have been great advancements in the understanding and modeling of proteins embedded in the membrane (1–3). One of the first lessons from experiment was that membrane structural and mechanical properties can induce proteins to undergo conformational changes to carry out their function. Early experiments on the antibiotic ion channel forming peptide gramicidin A showed that the thickness of the membrane drives dimerization of the channels (4), whereas later experiments on the mechanosensitive channel MscL (5) showed that in-plane tension and the hydrophobic thickness of the membrane bias the opening and closing of MscL. In addition to the influences of membrane rigidity and thickness, further advancements in experimental techniques have shed light on how membrane shape is coupled to protein function, localization, diffusional properties, and protein-protein interactions (3). For instance, membrane curvature plays a crucial role in the mobility of proteins in the membrane (6). Curvature is thought to affect the probability of alamethicin conductance states (7) and to play an allosteric regulatory role for ion channel function of α-hemolysin (8). Moreover, proteins are not static. Proteins push back on the bilayer, potentially acting as shape remodeling elements that may even influence how cells carry out their biological function (9,10) For example, protein coats composed of COPI or COPII complexes have been associated with the distinct shapes of spherical vesicles that shuttle between the endoplasmic reticulum and Golgi (11), whereas the homotypic fusion of embedded proteins on opposing membranes is believed to induce endoplasmic reticulum tubular networks (12). Also, there is growing evidence that rows of transmembrane F-ATPase dimers are partially responsible for the complex folds of the cristae (inner mitochondrial membrane) (13,14), and recent experiments using electron microscopy and electron paramagnetic resonance of endophilin A1 show that vesiculation and tubulation are likely a function of the depth of protein insertion (15).

Submitted November 28, 2016, and accepted for publication March 27, 2017.

*Correspondence: michael.grabe@ucsf.edu

David Argudo, Neville P. Bethel, and Frank V. Marcoline all contributed equally to this work.

Editor: Markus Deserno.

http://dx.doi.org/10.1016/j.bpj.2017.03.040

Parallel to this experimental evidence, several theoretical efforts to study the interaction between transmembrane proteins and their host membranes have also emerged. Fully atomistic simulation (16), coarse-grained models (17), purely analytic continuum approaches (18), and hybrid models (19,20) have been developed to explain what is observed in experiment and to further explore these interactions beyond the spatial and temporal resolutions of current experimental techniques. A key characteristic of molecular dynamic simulations is the possibility of extracting a lateral pressure profile that describes the nonhomogeneous membrane stress inside a bilayer arising from hydrophobic, electrostatic, and steric interactions (21). The membrane stress profile can then be used to study the mechanical coupling between the protein and the bilayer but results are affected by the level of coarsening in the simulation (22). Protein-driven membrane deformations require system sizes and timescales that are challenging for fully atomistic simulation. Continuum approaches, however, are less computationally demanding and have proven to be an effective tool to study these systems (3). Numerous continuum models for the membrane exist, most of which predict the deformation of the membrane that minimizes the mismatch between the hydrophobic core of the membrane with the hydrophobic belt of amino acids around the protein (2,23–27). The models calculate the shape of membrane surfaces and also provide the resulting membrane compression and curvature energies.

Gramicidin-A function in the membrane has been well characterized using experimental techniques (4,28), and for this reason it serves as a model system for the validation of continuum and computational approaches. This antimicrobial, short peptide forms anchors in either upper and lower monolayers, and individual peptides come together to create a homodimer that spans the membrane. The ion channel is only functional as a dimer, and in thicker membranes, gramicidin must pinch the upper and lower leaflets to dimerize. For this reason, dimer formation is a function of the hydrophobic mismatch between the dimer hydrophobic region and the membrane hydrophobic thickness. Membrane bilayer energetics are related to the changes of the average gramicidin channel lifetimes (26,29), and this phenomenon provides experimentally measurable evidence of the underlying physical interactions between the membrane and the protein. Many groups have successfully studied these lifetimes using continuum membrane models (23–25,27,30,31). These theoretical approaches have provided deep insight into the effects of membrane elastic properties and protein boundary conditions on the energetics of the system and the equilibrium shapes of the membrane near the protein. Nevertheless, the majority of these continuum-based studies have represented the protein as an idealized cylinder lacking chemical detail. Consequently these continuum models have failed to reproduce outcomes of detailed atomistic studies (16,18,22). This observation has prompted the field to refine the continuum approaches and include atomistic detail (19,32,33), geometric effects (34,35), or both (20,36). For example, the Weinstein group (20,36) developed a novel method to account for deformations of the bilayer by noncylindrical shape inclusions. Their model represents the membrane as two uncoupled single sheets. They used a finite difference solver on a Cartesian grid where the membrane is represented by a continuum elastic model but the boundary conditions for the model are directly extracted from the membrane heights at the protein-membrane interface from molecular dynamics (MD) simulations. This coupling to observations from MD proved useful in quantifying the hydrophobic mismatch-driven remodeling of membranes by G protein-coupled receptors (20) and studying the coupling between membrane shape and conformational states of the bacterial leucine transporter (36). Similarly, Haselwandter and co-workers developed sophisticated analytic and numerical treatments of the membrane-protein contact boundary to explore the influence of protein shape on the membrane deformation energies of MscL (34,35,37). Those authors used a continuum elastic representation of the membrane together with mixed finite element formulation to solve for the membrane energies. Although currently their methods do not include atomistic detail, their approach yields rapid numerical convergence for complex domains and have successfully been applied to study the relations between the shape of MscL and the supramolecular architecture of MscL lattices and clusters (35).

Here, we present a hybrid continuum-atomistic model that can describe membrane deformations induced by membrane proteins of arbitrary shape. The model uses the structural information from the protein inclusion (19,32,38) together with a finite volume, continuum representation of the membrane (39). In contrast to previous models (19,20,35), we include protein chemistry and geometrical effects, but our methods are self-consistent and do not require any input from molecular dynamics. The finite volume numeric scheme for describing the membrane shape allows us to distort the grid near the protein interface, resulting in smooth membrane-protein boundaries and a distorted grid that increases the accuracy of our solver with fewer discrete elements than a Cartesian grid. The membrane is allowed to undergo asymmetric bilayer deformations, where the effects of possible redistribution of the membrane lipids near the inclusion are captured by the space-dependent behavior of the elastic moduli (27). The deformation profile is calculated by minimizing the sum of the elastic, electrostatic, and nonpolar energies. Incorporating all three energies provides a more sophisticated and realistic view of global membrane-protein energetics than provided by membrane-only models. In the next section, we derive our continuum model for bilayer deformations in response to the insertion of an integral protein. Then we validate our method by comparing membrane shapes produced by fully atomistic simulations of gramicidin with membrane shapes produced from our continuum calculations. Our model is able to accurately reproduce the membrane height profiles, boundary conditions, and protein orientation seen in our simulations. We discuss how care must be taken when producing average membrane surfaces from MD trajectories with a particular emphasis on periodic boundary effects and fluctuations in protein position. Finally, to illustrate the capability of our model to handle complex protein shapes, we study the membrane-induced deformations by the thermosensitive ion channel, TRPV1. These deformations significantly reduce the electrostatic penalties caused by exposing charged and polar residues to the membrane core.

MATERIALS AND METHODS

Model description

As in our previous works (19,32,38), the total energetic stability of the membrane-protein system is approximated as the following:

$$G^{T} = G^{(me)} + G^{(e)} + G^{(np)} + G^{(o)}, \tag{1}$$

where $G^{(me)}$ is the membrane elastic energy due to the shape distortions in the membrane, $G^{(e)}$ is the electrostatic penalty caused by inserting a charged protein into the low-dielectric environment of the membrane, $G^{(np)}$ is the nonpolar energy associated with burying protein surface area in the membrane (hydrophobic effect), and $G^{(o)}$ represents the orientational entropy cost of a protein constrained to only explore a subset of tilted configurations. We calculate the change in free energy of the protein-membrane system with respect to a reference state where the protein is completely in solution, far away from the undistorted (flat) membrane. For transmembrane proteins, the hydrophobic effect tends to be the largest component, and it stabilizes the protein in the membrane through the nonpolar energy $G^{(np)}$. Typically, $G^{(np)}$ is approximately three times larger than the electrostatic interactions $G^{(e)}$, which in turn tend to destabilize the protein; however, these two components can vary significantly depending on the size and charge makeup of the protein in question. Whereas $G^{(np)}$ and $G^{(e)}$ play the major role in determining the insertion energy, the membrane can still deform to accommodate a charged protein leading to an unfavorable elastic penalty $G^{(me)}$ that is approximately an order-of-magnitude smaller than $G^{(np)}$, in many cases. Finally, the orientational entropy $G^{(o)}$ has a very modest effect in stabilizing the protein. In this section, we outline the elements of our theory that allow us to account for arbitrary shape protein inclusions. First, we describe the general geometry of the protein-membrane system, and then we present the theory behind the membrane elasticity $G^{(me)}$ term in Eq. 1. For details on the energetic description on the nonelastic energetic terms ($G^{(e)} + G^{(np)} + G^{(o)}$), we refer the reader to our previous publications (3,19,32,38,40) and the Supporting Material.

Geometry: matched and unmatched regions

We consider a bilayer membrane made up of two monolayers (leaflets) of identical lipid composition with an embedded protein of arbitrary shape (a graphical representation is given in Fig. 1). Due to the nonuniform cross-sectional area of the protein, the area projections in the *x-y* plane of the upper and lower leaflets do not coincide (see Fig. 1 *B*). The projected area in the *x-y* plane covered by the upper leaflet is denoted Ω^{+}, and it is described by the field variable $h^{+}(x,y)$. Similarly, Ω^{-} is the projected area of the lower leaflet, where the leaflet's height is given by $h^{-}(x,y)$. Because the leaflets do not coincide at all *x-y* values, it is useful to characterize the matched and unmatched regions between the projected areas. The region $\Omega_M = \Omega^{+} \cup \Omega^{-}$ is defined as the matched *x-y* region, where h^{+} and h^{-} are well defined. On the other hand, $\Omega_1 = \Omega^{-} - \Omega_M$ represents the unmatched region in the *x-y* plane where only the lower leaflet variable h^{-} is well defined, while $\Omega_2 = \Omega^{+} - \Omega_M$ represents the unmatched area where only the upper leaflet variable h^{+} is well defined. Finally, we define the shape variables $u^{\pm}$ as the difference between the height $h^{\pm}$ of the upper and lower leaflets with respect to the flat equilibrium height of the membrane $h_0 = L_0/2$ as follows:

$$u^{\pm}(x_1, x_2) = \left(h^{\pm} \mp \frac{L_0}{2}\right). \tag{2}$$

Membrane deformation energy $G^{(me)}$

As mentioned earlier, $G^{(me)}$ represents the elastic energetic penalty due to membrane deformation in the presence of an inserted protein. We chose to use a continuum theory to describe the shape deformations of the bilayer by considering independent variables for each monolayer (23,38). For a general configuration (e.g., Fig. 1) where there are two unmatched regions Ω_1 and Ω_2, we define the total membrane free energy as the sum of the independent contributions of each monolayer, as follows:

$$G^{(me)} = G_M^{(me)} + G_1^{(me)} + G_2^{(me)}, \tag{3}$$

where ${G_M}^{(me)}$ is the elastic energy contribution of the two monolayers over the region Ω_M where both $u^{+}(x,y)$ and $u^{-}(x,y)$ are defined, ${G_1}^{(me)}$ is the contribution over the unmatched region Ω_1 where only u^{-} is defined,

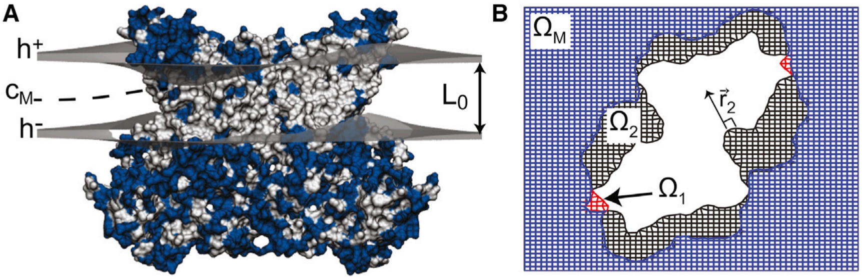

FIGURE 1 Continuum membrane model for proteins of arbitrary shape. (*A*) Shown here is a wide view of membrane deformation around an embedded membrane protein from the continuum model. The membrane headgroup-tail interfaces are shown as gray surfaces, where $h^{+}(x,y)$ describes the upper leaflet shape and $h^{-}(x,y)$ describes the lower leaflet shape. The membrane dividing (compression) surface C_M is shown by the dashed line and the unperturbed membrane thickness is labeled L_0. The protein is shown in molecular surface representation. Residues are blue and white for hydrophilic and hydrophobic residues, respectively. (*B*) Given here is the top-down view of grid used in membrane solver. The blue area denotes the region where the upper and lower leaflets are matched Ω_M, meaning $u^{+} = h^{+} - L_0/2$ and $u^{-} = h^{-} + L_0/2$ are defined. The red areas near the boundary correspond to the unmatched Ω_1 region where only the lower leaflet variable u^{-} is defined. The black areas near the boundary represent the unmatched region Ω_2 where only the upper leaflet variable u^{+} is defined and $\vec{r}_2$ is the normal vector to the curve describing the protein/upper-monolayer interface. For illustrative purposes, the grid spacing has been enlarged and truncated around the protein. To see this figure in color, go online.

and $G_2^{(me)}$ is the contribution over unmatched Ω_2 where only u^+ is defined. The energy $G_M^{(me)}$ over the matched region Ω_M is given by the following (23):

$$\begin{aligned} G_M^{(me)} = {} & \frac{1}{2}\int_{\Omega_M} \underbrace{\frac{K_c}{2}\left[\left(\nabla^2 u^+ + J_0^+\right)^2 + \left(\nabla^2 u^- - J_0^-\right)^2\right]}_{\text{Mean Curvature-Bending}} dxdy \\ & + \frac{1}{2}\int_{\Omega_M} \underbrace{\frac{\alpha}{2}\left[\left(\vec{\nabla} u^+\right)^2 + \left(\vec{\nabla} u^-\right)^2\right]}_{\text{Surface tension}} dxdy \\ & + \int_{\Omega_M} \underbrace{\frac{K_a}{L_0^2}\left[\left(u^+ - c_M\right)^2 + \left(u^- - c_M\right)^2\right]}_{\text{Compression}} dxdy \\ & + \int_{\Omega_M} \underbrace{\frac{K_G}{2}\left[\left(\frac{\partial^2 u^+}{\partial x^2} \times \frac{\partial^2 u^+}{\partial y^2}\right) - \left(\frac{\partial^2 u^+}{\partial x \partial y}\right)^2 + \left(\frac{\partial^2 u^-}{\partial x^2} \times \frac{\partial^2 u^-}{\partial y^2}\right) - \left(\frac{\partial^2 u^-}{\partial x \partial y}\right)^2\right]}_{\text{Gaussian Curvature}} dxdy, \end{aligned} \tag{4}$$

where we have used the $u^{\pm}$ definitions in Eq. 2, the "+" refers to the upper monolayer and "−" the lower one, and factors of two are present due to a monolayer versus bilayer description. K_c is the bilayer bending modulus, α is the surface tension parameter, K_a is the bilayer area compression modulus, and K_G is the bilayer Gaussian modulus. The variables $J_0{}^+$ and $J_0{}^-$ are the spontaneous curvatures of the upper and lower leaflets, respectively. We have defined $J_0{}^{\pm}$ using the standard sign convention, such that a lipid at equilibrium with a positive spontaneous curvature is one with a large headgroup with a preference for a micelle geometry (41). Above, we have written the compression term as a function of the surface $c_M(x,y)$ separating the two leaflets (Fig. 1 *A*). For more details, we refer the reader to the literature (42–45) and the Supporting Material accompanying this article.

Minimizing the free energy in Eq. 4 with respect to $c_M(x,y)$ yields: $c_M = (u^+ + u^-)/2$, which corresponds to the midplane of the bilayer (42). Using this last result for c_M in the compression term of Eq. 4 recovers the liquid crystal-based energy expression proposed by Huang (23) and used in our previous works (19,32,38).

The functional forms of $G_1{}^{(me)}$ and $G_2{}^{(me)}$ over the unmatched regions are analogous to the expression Eq. 4, but each term only has contributions from a single leaflet. Where the in-plane areas of the inserted protein do not match in the upper and lower leaflets there are projected regions where the bilayer midplane does not exist. For such scenarios, the lipids in opposing monolayers will still be compressed against a dividing surface $c(x,y)$, which is constrained by the protein's geometry. We define the field variables $c_1(x,y)$ and $c_2(x,y)$ as the dividing (compression) surface over regions Ω_1 (upper monolayer) and Ω_2 (lower monolayer), respectively. The functions $c_1(x,y)$ and $c_2(x,y)$ are protein specific, but for transmembrane proteins spanning both leaflets, where the mismatched region is small compared to the total protein surface area projection (i.e., gramicidin, TRPV1), we propose an approximation, as follows:

$$c_1 = \frac{u^- + u_B^+}{2} \quad \text{and} \quad c_2 = \frac{u^+ + u_B^-}{2}, \tag{5}$$

where $u_B^+(x,y)$ is the boundary condition of the field variable u^+ enforced at the contact curve between the upper leaflet and the protein. Similarly $u_B^-(x,y)$ is the boundary condition of u^- at the contact curve between the lower leaflet and protein. Equation 5 assumes that the monolayer dividing surfaces c_1 and c_2 are not heavily distorted with respect to c_M and can be approximated by extending the bilayer midplane $c_M = (u^+ + u^-)/2$ by using the boundary values $u_B^{\pm}$ in regions where either the upper or lower leaflets are not defined. Equation 5 ensures that the resulting surface dividing the two monolayers is continuous in space. For more detail, please refer to the Supporting Material.

We can write the free energy contribution $G_1{}^{(me)}$ over region Ω_1, as follows:

$$\begin{aligned} G_1^{(me)} = {} & \frac{1}{2}\int_{\Omega_1} \frac{K_c}{2}\left(\nabla^2 u^- - J_0^-\right)^2 + \frac{\alpha}{2}\left(\vec{\nabla} u^-\right)^2 dxdy \\ & + \int_{\Omega_1} \frac{K_a}{L_0^2}\left(c_1 - u^-\right)^2 + \frac{K_G}{2}\left(\frac{\partial^2 u^-}{\partial x^2} \times \frac{\partial^2 u^-}{\partial y^2} - \left(\frac{\partial^2 u^-}{\partial x \partial y}\right)^2\right) dxdy, \end{aligned} \tag{6}$$

and the contribution $G_2{}^{(me)}$ over region Ω_2, as follows:

$$\begin{aligned} G_2^{(me)} = {} & \frac{1}{2}\int_{\Omega_2} \frac{K_c}{2}\left(\nabla^2 u^+ + J_0^+\right)^2 + \frac{\alpha}{2}\left(\vec{\nabla} u^+\right)^2 dxdy \\ & + \int_{\Omega_2} \frac{K_a}{L_0^2}\left(u^+ - c_2\right)^2 + \frac{K_G}{2}\left(\frac{\partial^2 u^+}{\partial x^2} \times \frac{\partial^2 u^+}{\partial y^2} - \left(\frac{\partial^2 u^+}{\partial x \partial y}\right)^2\right) dxdy. \end{aligned} \tag{7}$$

As before, we have assumed that both monolayers have equal elastic moduli, and we have expressed the energy contributions in terms of bilayer moduli to be consistent with Eq. 4.

Membrane equilibrium configurations

The membrane equilibrium shape equations associated with the elastic energy $G^{(me)}$ are determined by minimization of Eqs. 4–7 resulting in the following Euler-Lagrange equations:

$$\nabla^4 u^+ - \nabla^2 J_0^+ - \gamma \nabla^2 u^+ + \beta\left(u^+ - u^-\right) = 0, \text{ in } \Omega_M, \tag{8}$$

$$\nabla^4 u^- + \nabla^2 J_0^- - \gamma \nabla^2 u^- + \beta\left(u^- - u^+\right) = 0, \text{ in } \Omega_M, \quad (9)$$

$$\nabla^4 u^- + \nabla^2 J_0^- - \gamma \nabla^2 u^- + \frac{\beta}{2}\left(u^- - u_B^+\right) = 0, \text{ in } \Omega_1, \quad (10)$$

$$\nabla^4 u^+ - \nabla^2 J_0^+ - \gamma \nabla^2 u^+ + \frac{\beta}{2}\left(u^+ - u_B^-\right) = 0, \text{ in } \Omega_2, \quad (11)$$

where we have made use of Eq. 5 and defined the following:

$$\gamma = \frac{\alpha}{K_c}, \;\; \beta = \frac{2K_a}{L_0^2 K_c}, \;\; u_B^{\pm} = \left(h_B^{\pm} \mp \frac{L_0}{2}\right). \quad (12)$$

Under the assumption of constant or vanishing spontaneous curvatures $J_0^{\pm}$, we recover the equations of our earlier work (19,32,38). Note that Gaussian terms do not appear in the Euler-Lagrange equations Eqs. 8–11. The Gaussian curvature terms can be transformed into boundary integrals by means of the divergence theorem (46,47) and consequently do not contribute to the shape equations of the system.

The equilibrium equations Eqs. 8–11 can be readily solved for u^+ and u^- given a suitable set of boundary conditions. First, it is physically reasonable to assume that far away from the protein the perturbation effects on the membrane deformations vanish. As the perturbations vanish, the membrane asymptotically approaches its unstressed equilibrium configuration, as follows:

$$u^+ = u^- = \vec{\nabla} u^+ = \vec{\nabla} u^- = 0 \text{ far away from inclusion.} \quad (13)$$

Meanwhile, at the protein-membrane boundary, we impose the following fixed set of boundary conditions:

$$\begin{aligned} u^+ = u_B^+, \;\; u^- = u_B^-, \;\; \vec{\nabla} u^+ \times \vec{r}_2 = S^+, \\ \text{and} \quad \vec{\nabla} u^- \times \vec{r}_1 = S^-, \end{aligned} \quad (14)$$

where $\vec{r}_1$ is the normal vector to the curve describing the protein/lower-monolayer interface and $\vec{r}_2$ is the corresponding vector at the protein/upper-monolayer interface (see Fig. 2). This last set of conditions in Eq. 14 depends on the geometry and atomic structure of the protein, and for this reason is optimized by an iterative procedure that attempts to minimum the total energy of the system, G^T (32,38). Details on the minimization procedure are in the next section.

Although we have chosen to use the fixed boundary conditions given in Eq. 14, there are other alternative conditions that still satisfy Eqs. 8–11. In the Supporting Material, we address in detail the treatment of boundary conditions for elastic continuum models and the proposed version of a hybrid continuum-atomistic model.

Minimization of the total energy G^T

In 2013, Lee et al. (18) suggested that elastic continuum descriptions fail to reproduce the membrane deformations near the protein boundary observed in MD simulations. The disparity between MD and continuum methods has been argued to result from the lack of explicit chemical and geometrical effects of the inserted protein (3,18,20). The contact conditions between membrane and protein will have a large effect not only on the membrane deformation energy but also on nonpolar and electrostatic penalties. Therefore, determining the minimum energy of the system G^T (Eq. 1) requires a

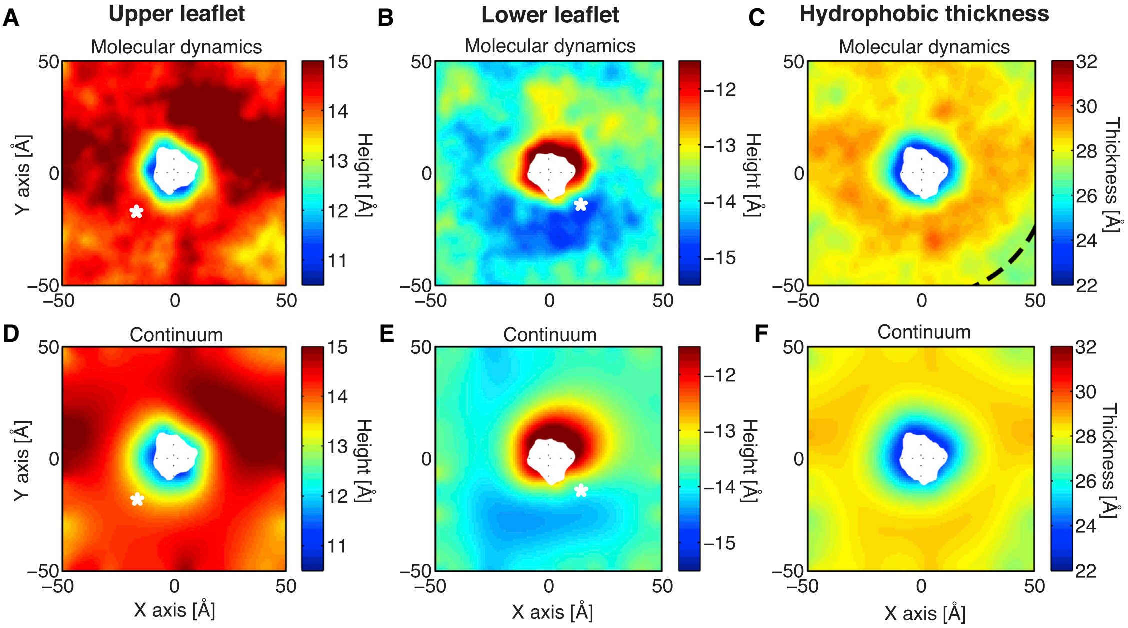

FIGURE 2 Comparison of protein-induced membrane deformations from molecular dynamics and continuum elasticity. (*A–C*) Shown here are the average membrane height profiles for the upper leaflet (*A*), lower leaflet (*B*), and hydrophobic thickness (*C*) from one 250-ns MD simulation of gramicidin in a POPC bilayer. (*D*)–(*F*) show the corresponding continuum membrane surfaces. For the continuum calculations (*D*)–(*F*), we used boundary conditions at the protein-membrane boundary and at the edges of the box that were extracted from the MD data in (*A*)–(*C*). The region where the membrane is compressed near the protein *(compression ring)* can be clearly seen in the hydrophobic mismatch panels of both the MD (*C*) and continuum calculations (*F*). Dashed arc line in (*C*) shows a 55 Å radial distance measured from the center of the protein. White asterisks show the location of maximum difference between leaflet heights calculated using simulation (*A*) and (*B*) when compared to continuum (*D*) and (*E*). For reference, in Fig. S8 we show the gramicidin-induced membrane deformations calculated using our hybrid-atomistic model without any input from MD. To see this figure in color, go online.

thoughtful choice of the prescribed boundary conditions at the protein-membrane interface. Our hybrid-continuum approach is equipped to determine the correct boundary conditions. We search for the optimal set of fixed boundary conditions Eq. 14 that minimize the total energy G^T and consequently play the key role in coupling the elastic and nonelastic effects (see Eq. 1). To find the optimal value of the displacement boundary conditions u_B^+ and u_B^-, we use a simulated annealing algorithm (48), where an iterative search is performed over all displacement parameters to obtain the membrane shape that minimizes G^T. The displacement boundary conditions are further optimized using Powell's method (49), then the slope boundary conditions are optimized using a Nelder-Mead simplex method (50). The Powell and Nelder-Mead optimizations are performed one more time to ensure convergence. We express the variables u_B^+ and u_B^- in Fourier series representation of order n (three or higher) where the search is over the $(2n+1)$ amplitude coefficients. The upper and lower slope variables, S^+ and S^-, are set as proportional to the upper and lower displacement boundary conditions, as follows:

$$S^+ = \alpha^+ u_B^+, \quad S^- = \alpha^- u_B^-, \tag{15}$$

where α^+ and α^- are the scalar parameters that are optimized. This simplification reduces the parameter space and the search time. More information can be found in Callenberg (48).

Identifying the membrane-protein contact curve

Within the dual monolayer framework, there are two contact curves—one for the upper leaflet and one for the lower leaflet. These curves represent the lipid excluded surface, which is the surface of closest contact between a spherical lipid probe and the protein atoms (51). To identify these curves, we first erect a flat Cartesian grid for the upper and lower leaflets, and then use level set theory to move grid points near the membrane-protein surface onto the boundary curve representing the lipid excluded surface (39). The mathematical details on how to obtain the distorted grid representing the monolayer surfaces with geometrically accurate boundary curves can be found in Wolgemuth and Zajac (39).

For both upper and lower leaflets, we define the smooth curve $C(x,y)$ that represents the lipid-excluded surface. Next, we find the level set function $L(x,y)$ (isocontour) rendering the signed minimum distance from every coordinate point (i,j) in the Cartesian grid to the curve $C(x,y)$. Therefore, the interface $C(x,y)$ is represented implicitly by the zero of the level set function $L(x,y) = 0$ and the unit normal to the curve $C(x,y)$ is given by the following:

$$\vec{r} = -\frac{\vec{\nabla} L(x,y)}{\left|\vec{\nabla} L(x,y)\right|}. \tag{16}$$

Fig. 1 shows the unit vector $\vec{r} = \vec{r}_2$ corresponding to the upper leaflet. Next, from the distance map $L(x,y)$ we identify the set B of all Cartesian grid points (i_B, j_B) within one Cartesian grid-edge length g_l of the curve C as follows:

$$B = (i_B, j_B) \text{ for } (i,j) \text{ satisfying } |L(i,j)| \leq g_l. \tag{17}$$

The collection of points in set B define the curve that most closely describes each leaflet boundary curve in a Cartesian grid. Finally, we distort the Cartesian grid points at the boundary by spatially moving all points in set B from their initial position $\vec{R}(i_B, j_B)$ onto the curve $C(x,y)$ using the following transformation:

$$\vec{R}_D(i_B, j_B) = \vec{R}(i_B, j_B) + L(i_B, j_B)\vec{r}, \tag{18}$$

where the new position vector $\vec{R}_D(i_B, j_B)$ describes the location of the distorted grid points representing the protein-membrane interface. In Eq. 18 the function $L(i_B, j_B)$ tells how far the points (i_B, j_B) in the regular Cartesian grid are from the curve C, while $\vec{r}$ tells the direction in which the position vector $\vec{R}$ needs to be displaced. One of the convenient features of this procedure is that the distorted grid (see Fig. 1) retains four-point connectivity and results in smooth boundaries (39). As with all numeric solutions of PDEs, an accurate description of the boundary is important for faithfully representing the shape of the system and properly applying boundary conditions. Once the boundaries are established, we solve the shape equations (Eqs. 8–11) using a finite volume method. Details of the numerical procedure can be found in Wolgemuth and Zajac (39).

Continuum model parameters

Here, we only consider homogeneous POPC membrane systems, and we have summarized the elastic and continuum parameters used throughout our calculations in Table 1. We assume the area compression modulus in the bulk for the upper and lower monolayers $K_{a,m}^{\pm}$ is half of the reported area compression modulus of the bilayer ($K_{a,B}$). This condition is justified over the bulk region Ω_M if we assume a constant and equal density of lipids per leaflet (see Supporting Material). We point out that although constant elastic rigidity is commonly used in continuum elastic models of the membrane (3), this assumption likely breaks down near the protein interface (18,27). From a physical point of view, one can expect spatial changes of the elastic constants due to limitation on the mobility and packing of the lipid molecules near the inclusion (shell hardening) (17,22,25–27). For this reason, it has been previously suggested that the common assumption of constant elastic parameters might be an oversimplification at the shorter length scales of a protein-membrane system (25). Partenskii and Jordan (27) implemented a model where values of the elastic constants near the inclusion are larger than the values in the bulk. In their work, this shell hardening effect has a decay length (~15 Å) comparable to the width of lipid molecules. In their work the bending and compression moduli are both increased near the protein, but the authors found that only the perturbation

TABLE 1 Elastic Membrane Material Properties Specific to POPC and Prescribed Parameters for All Continuum Calculations

Parameters	Values	Reference
Membrane thickness (L_0)	28.5 Å	Kim et al. (16)
Surface tension (α)	3.00×10^{-13} N/Å	Latorraca et al. (32)
Bending modulus (K_C)	8.5×10^{-10} NÅ	Kim et al. (16)
Gaussian modulus (K_G)	$\sim -0.9 \times K_c$	Hu et al. (54)
Shell hardening factor[a] (Θ)	~4.27	Partenskii and Jordan (27)
Area compression modulus (bulk)[a] ($K_{a,B}$)	2.13×10^{-11} N/Å	Latorraca et al. (32)
Protein dielectric (ε_p)	2.0	Latorraca et al. (32)
Membrane dielectric (ε_{hc})	2.0	Latorraca et al. (32)
Headgroup dielectric (ε_{hg})	80.0	Latorraca et al. (32)
SASA prefactor for nonpolar energy (a)	0.028 kcal/(mol•Å^2)	Sitkoff et al. (91)

[a] We have used nonuniform values of the compression modulus K_a (see Supporting Material). For the remaining parameters necessary for the electrostatic calculations (i.e., electrostatic grid dimensions), we use the same values presented in our previous publication (32).

of the compression bilayer constant K_a has a significant effect on the membrane energy. Comparison to gramicidin experiments showed that the compression modulus is ~5 times larger at the protein-membrane boundary than in the bulk ($K_{a,B}$) (27). In this model, we have incorporated shell hardening through a spatially dependent compression modulus $K_a^{\pm}(x,y)$ that is greatest at the protein-membrane boundary, and exponentially decays to the bulk monolayer value ($K_{a,m}^{\pm}$) as distance increases. Hardening primarily affects the first and second lipid shells surrounding the protein (for detail, see Supporting Material). We point out that in this model the function $K_a^{\pm}(x,y)$ can be arbitrary, and this does not change the governing Euler-Lagrange equations Eqs. 8–11. As in our previous work (32), we found that the surface tension (α) does not contribute significantly to the energy and for this reason we assume it to be a constant over all space. Finally, the last integral term in Eq. 4 is the Gaussian curvature energy contribution. In our problem, the membrane does not change topology between the initially flat surface and final distorted surface because both states include the protein hole. In addition to topological changes, the Gaussian term can be formally shown to contribute only through the boundary effects (24,47,52,53). When using fixed boundary conditions, as we do here, the equilibrium shape is independent of the Gaussian term, but the total energy G^T of any given configuration still depends on the Gaussian curvature. Consequently, this term will affect the search for the optimal equilibrium shape as described in Minimization of the Total Energy G^T. We have chosen to use Gaussian modulus K_G values from simulation (54,55), which are in reasonable agreement with reported experimental values. Also, in writing our energies we have assumed the Gaussian monolayer modulus to be half of the measured bilayer modulus K_G. This assumption is justified in our calculation, given that we use zero spontaneous curvature for each monolayer. In general, the relation between the monolayer and bilayer Gaussian curvature moduli has a correction term involving the monolayer spontaneous curvature and the position of the monolayer pivotal plane (41,56).

We point out that our model, like any continuum membrane representation, is limited by the phenomenological nature of the parameters describing the membrane mechanical properties (41). Experiments have shown that there are still uncertainties regarding the specific values of mechanical parameters (57,58), and the MD reported values do not always agree with experiment (59,60). In this work, we constrain ourselves to a smectic liquid-crystal model (23) where the mechanical parameters (Table 1) have been picked from the gramicidin-POPC literature (16,18), keeping in mind that our goal is a comparison between our hybrid continuum model and MD simulations.

Simulation methods

Simulations were prepared using the NMR gramicidin structure (PDB: 1JNO) (61). With CHARMM-GUI (62), the structure was inserted into a 97 × 97 Å^2 POPC membrane, and solvated with TIP3P water molecules (63), and 150 mM KCl. The total system size was 38,876 atoms. The system was run in the software NAMD (http://www.ks.uiuc.edu/Research/namd/) (64) using the CHARMM36 lipid force field (http://mackerell.umaryland.edu/charmm_ff.shtml) (65) with an anisotropic Nosé-Hoover-Langevin barostat and Langevin thermostat. Equilibration and production simulations were carried out using the default parameters provided by CHARMM-GUI (http://www.charmm-gui.org/). Two independent gramicidin simulations were separately prepared and run for 250 ns each, and another membrane-only simulation was prepared and run for 100 ns.

The hydrophobic interfaces of the upper and lower leaflets were averaged over time to obtain a single MD-generated membrane surface to compare with the continuum predictions. The goal of such averaging is to provide a physically accurate representation of the equilibrium shape of the membrane, but we note that the average of a solution set is not necessarily a solution itself. That is, averaging the membrane surface may produce physically unrealistic shapes. To reduce possible artifacts from averaging, we used an interpolation method. When comparing membrane surfaces between MD and our continuum model, each frame from MD was aligned to the initial snapshot by centering the protein. Then the upper and lower surfaces were interpolated from the C2 carbon atoms of the POPC acyl chains (66) using a cubic spline method. After the alignment, the upper and lower surfaces were averaged over all frames. When comparing the predicted boundary conditions of our continuum model to MD, the protein was further aligned by rotating in the *x-y* plane to minimize the root mean square deviation of the protein backbone. Because the continuum model assumes the membrane lies in the *x-y* plane, the simulations were only allowed to rotate about the *z* axis during the alignment. Other rotations were not allowed because this would rotate the membrane out of the *x-y* plane. Additional details are provided in the Supporting Material.

RESULTS AND DISCUSSION

Gramicidin induces asymmetric deformations

We first applied our model to study the membrane deformations created around the antibacterial ion channel gramicidin. This protein is often used to explore protein-membrane interactions, because its ability to conduct ions is intimately connected to the properties of the membrane (4), and experimental studies have demonstrated membrane thinning/thickening at the protein interface (28). Continuum elastic models have proven useful in predicting the energetics of gramicidin induced deformations and using these energies to accurately estimate open channel lifetimes (18,26,67). All of these models use a simplified cylindrical description of gramicidin leading to radially symmetric membrane distortions. In 2012, Kim et al. (16) rigorously compared the continuum distortions to those observed from all-atom molecular dynamics simulations. Interestingly, despite their reliability in determining channel function, the authors noted that simplified continuum elastic models fail to reproduce the deformations observed in simulation (16).

We chose to revisit this analysis using a more accurate treatment of the channel chemistry and geometry to determine if these features could overcome the deficiencies inherent in simpler continuum models. We started by running two independent simulations of gramicidin in a 100 × 100 Å^2 membrane patch of POPC membrane for 250 ns each (500 ns total). The average membrane deformation profiles from the two MD simulations are shown in Fig. 2, *A–C*. Similar to previous studies (16,22), we observe highly nonsymmetric deflections in the upper and lower leaflets with respect to the bilayer midplane (Fig. 2, *A* and *B*). The greatest distortion in the upper leaflet is the blue region adjacent to the protein (Fig. 2 *A*), whereas the greatest distortion in the lower leaflet is the red region adjacent to the protein but on the opposite side (Fig. 2 *B*). Both distortions result in membrane compression as summarized in the plot of the membrane hydrophobic thickness (Fig. 2 *C*). The bulk, equilibrium POPC thickness is 28.5 Å, and at the protein the membrane is 22 Å whereas along the outer edge (~50 Å away) the membrane thickness is between 27 and 30 Å. The thickness at the middle of the simulation box edges is ~1 Å thicker than the equilibrium value indicating that it has not returned to equilibrium. However, in the corners the membrane is quite close to the bulk value. This observation indicates that care must be taken when interpreting protein-membrane coupling on small patches of membrane where the boundary conditions of the box enter, as has been highlighted previously (32,68).

As a first test of our continuum model, we asked whether it could reproduce the membrane surfaces observed in fully atomistic simulation if we extracted the boundary conditions at the membrane-protein interface and the outer boundary directly from the simulation. Thus, we focused only on the elastic component of our model ($G^{(me)}$), ignoring for now the electrostatic ($G^{(e)}$) and nonpolar ($G^{(np)}$) contributions. For consistency between the MD calculations and our continuum approach, we calculated the most probable protein orientation from MD, and then used the same orientation in our continuum calculations. To obtain the boundary conditions, we first identified the boundary curve of a single snapshot from the MD simulations using the level set method described earlier. The displacements at the boundaries were found by interpolation from the MD membrane surfaces, and the slope boundary conditions were calculated by taking the dot product of the surface gradient and the normal of the boundary. The corresponding continuum surfaces are plotted in Fig. 2, *D*, *E*, and *F*, under their respective averaged surfaces from MD (Fig. 2). In the solution domain, the continuum membrane surfaces match remarkably well with the surfaces seen in MD, indicating that continuum elastic models can accurately describe membrane distortions on protein-sized length scales. Both methods predict very similar damped oscillating profiles where the membrane first pinches down by ~4 Å near the protein forming a ring where the membrane is compressed (compression ring), then the membrane expands to overshoot the bulk value before finally returning to equilibrium values at the corners of the simulation box (Fig. 2). The upper leaflet height in Fig. 2 *D* differs by <1.0 Å with the MD results (Fig. 2 *A*) over the entire surface, and the mean absolute deviation between both surfaces is only 0.2 Å. Similarly, the continuum and MD surfaces for the lower leaflet are at most 1.5 Å different from each other with a mean absolute deviation of 0.3 Å. The most notable difference between the continuum calculations and the MD simulations is the size of the compression ring around the protein (Fig. 2, *C* and *F*). The ring extends radial from the center of the protein for 25–30 Å in the continuum calculations, but only 20–25 Å in the MD simulations.

It has been suggested that the bilayer becomes harder near embedded proteins (27), and in Fig. 2, we used a variable compression modulus with a hardening factor $\Theta = 4.27$ (taken from Partenskii and Jordan (27)) to capture this effect. We found that this hardening factor is essential for modulating the radial extent of the membrane compression ring. In the absence of hardening ($\Theta = 1$), gramicidin-induced distortions extend over a larger ring (30–35 Å) (data not shown), which results in a poorer match with what is observed in MD. Increasing the hardening factor beyond 4.27 produces an even better match to MD, but the deformation energy increases significantly and there is no experimental estimate of Θ for the gramicidin-POPC system.

Continuum elastic models readily provide estimates of the membrane distortion energy, whereas MD simulations do not, and extracting boundary conditions from MD to solve continuum elasticity equations to determine deformation energies has been used previously (13,20). The gramicidin membrane configuration in Fig. 2 produces a POPC membrane distortion energy of 10.4 kcal/mol. The energy is equally shared by the upper and lower leaflets, with the compression mode accounting for most of the energetic penalty (49%), followed by the mean curvature effects (33%) and Gaussian curvature effects (17%). As in previous studies, we find that the surface tension has a negligible contribution (<1%) (18,19,23,25,27). Returning to the full energetic calculation of our implicit membrane model, the elastic deformation (~10 kcal/mol) and electrostatic component (~25 kcal/mol) are unfavorable, but overall gramicidin is stabilized in the membrane by the nonpolar energy (~−83 kcal/mol), which arises from the significant fraction of buried protein surface area.

Predicting protein orientation in the membrane

Next, we wanted to determine if we could use our full continuum energy model to predict the orientation of gramicidin in the membrane. The full model (Eq. 1) includes electrostatic and nonpolar contributions in addition to the membrane deformation energy. The boundary conditions at the membrane-protein interface are extracted from the protein structure using our proposed methodology in Minimization of the Total Energy G^T. Starting with the long axis of the protein aligned with the *z* axis and the protein center of mass in the middle of the membrane, we carried out a search over the upper and lower membrane-protein contact curves to determine the optimal membrane deformation profile that minimizes the total energy. We applied flat outer boundary conditions on a 150 × 150 Å^2 outer boundary, far enough from the protein that our MD simulations predicted that the membrane should return to its equilibrium value. Once the optimal membrane contact curve and energy were determined for this one orientation, we scanned through a series of tilt and rotation angles and identified the minimum energy membrane configuration for each orientation, $E(\theta, \rho)$. Tilting of gramicidin breaks the bilayer symmetry about the midplane, leading to different membrane-protein interfaces in the upper and lower leaflets. Our model and numeric scheme is equipped to handle symmetry breaking that arises from complex protein shape as well as protein orientation in the membrane caused by tilt. With these energies, we created a two-dimensional pseudo-histogram of gramicidin orientation, $H(\theta, \rho)$, using the relation: $H(\theta, \rho) = \exp(-E(\theta, \rho)/k_B\mathrm{T})$. The map generated by our continuum model provides good agreement with the histogram obtained from simulation (Fig. 3, *A* and *B*). Additionally, the minimum energy orientation matches remarkably well with the average orientation seen in simulation (Fig. 3, *A* and *B*). The model predicts an optimal orientation of 10° tilt and 77° rotation, while the MD predicts 12.5° tilt and 62° rotation. The orientational entropy term $G^{(o)}$ slightly stabilizes the predicted tilted configuration by ~1 kcal/mol with respect to the vertical configuration, which is expected given the increase in accessible states for moving off axis. For both the MD and the hybrid continuum-atomistic model, the protein orients to maximally expose the hydrophilic indole nitrogens on the tryptophan residues. Because the POPC bilayer is thicker than gramicidin, the membrane must also pinch to expose these hydrophilic groups. We hypothesized, therefore, that this orientation would no longer be the most energetically favorable if the membrane was very stiff. To test this idea, we carried out the same search with a nondeformable membrane. The predicted orientation no longer matches MD or our deformable membrane model (Fig. 3, *C*), demonstrating that membrane deformation is necessary to predict protein orientation in the membrane in this instance.

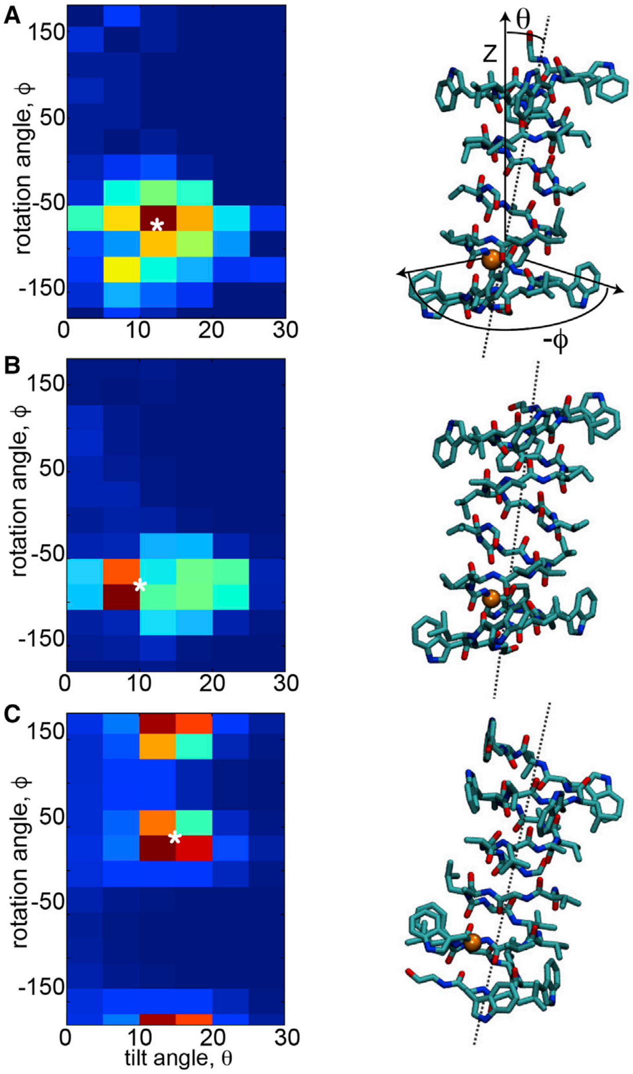

FIGURE 3 The continuum model predicts the correct protein orientation in the membrane. Given here is the orientation of gramicidin in the membrane predicted from MD simulations (*A*), our hybrid continuum-atomistic model (Eq. 1) (*B*), and the continuum model without membrane bending (*C*). In all panels, the heat map on the left shows the probability of finding gramicidin at specific tilt θ and rotation ρ-angles, where θ is the angle between the z axis and the long axis of the helix, and ρ corresponds to rotation about the long axis of the channel. To define the rotation ρ, we use as reference points the projection of the z axis together with the vector formed by the helical principal axis and the C_α position in residue W9 (16). The most probable configuration has been marked with a white asterisk (*). The right panel shows the protein configuration corresponding to the most probable configuration, as well as the pictorial description of θ and ρ. Probabilities were obtained by calculating the energy at each orientation, then using Boltzmann weighting to convert the energies to probabilities. To see this figure in color, go online.

Predicting the membrane-protein contact curve

Next, we wanted to determine if our hybrid continuum-atomistic model (Eq. 1) could actually predict the shape of the membrane-protein contact curve observed in the MD simulations. First, we investigated our two independent MD simulations to determine if the contact curve is characterized by a single contour with very little variation, or if it fluctuates wildly, which would be impossible for our deterministic model to reproduce. Individually averaging the results from both simulations showed pronounced membrane pinching at the contact interface by as much as 2 Å at the upper leaflet and 2 Å at the lower leaflet (*solid green* and *blue curves* compared to the *constant dashed line*; Fig. 4), but there are subtle differences between the simulations because the membrane thickness varied in the azimuthal direction and it showed fluctuations over time. Calculating the SD of the contact curve in time revealed that it fluctuates up to 4 Å in both leaflets (*blue* and *green shaded intervals* in Fig. 4). The variance in the height arises from changes in side-chain rotamer conformation, changes in protein tilt and rotation angle, and thermal motion of the membrane-protein system. Thus, the average membrane surfaces and contact curves result from a superposition of many different protein configurations. With this in mind, we identified 32 snapshots from our MD simulations that populated the most probable bin in Fig. 3 *A*, and we used our continuum model (Eq. 1) together with the protein structure to calculate the optimal membrane boundary for each snapshot configuration. The average membrane-protein contact curves for the upper and lower boundary from these continuum calculations are shown in Fig. 4 where we see good agreement with both MD simulations (*dash/dotted line*). Moreover, Fig. 4 *C* shows one of the continuum solutions revealing that membrane-anchoring tryptophans are the primary

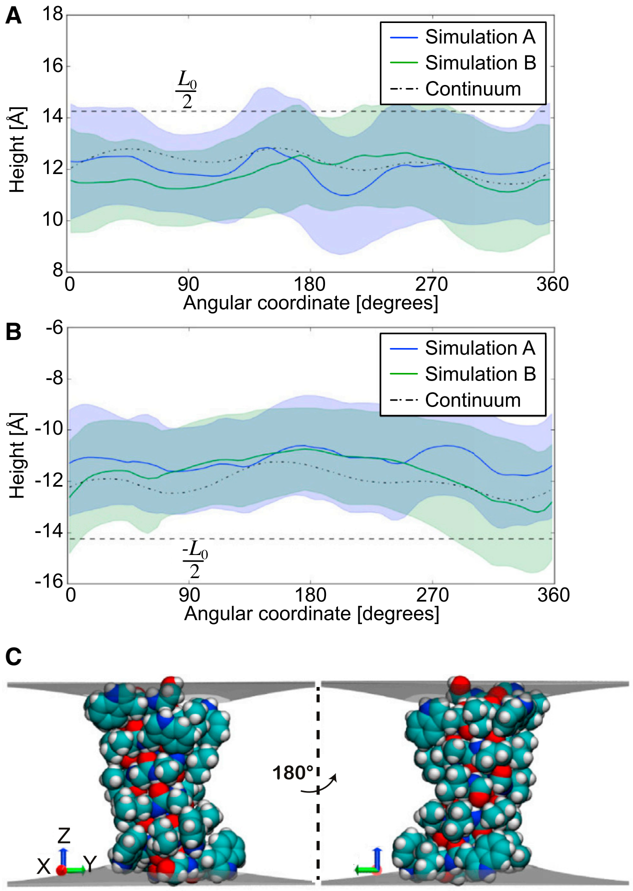

FIGURE 4 Comparison of protein-membrane boundary distortions from the continuum model and MD simulation. Given here are the membrane height values at the protein-membrane boundary for the upper leaflet (*A*) and lower leaflet (*B*). The dotted line corresponds to the average solution calculated from 32 protein snapshots by our continuum model. The blue and green solid lines are the average membrane height values from the two independent 250 ns MD simulations. The blue- and green-shaded regions correspond to MD solutions within 1 SD and the overlap between the blue- and green-shaded region has been highlighted in a darker color. The equilibrium height of the undeformed monolayer $L_0/2$ is shown by dashed lines. (*C*) Shown here are the membrane surface profiles calculated from the model. The angular coordinate in (*A*) and (*B*) are with respect to the x axis shown here. The protein-membrane boundaries align with the indole nitrogens of the tryptophans and the hydroxyl of the terminal ethanolamine. The right view corresponds to a 180° rotation about the z axis. To see this figure in color, go online.

determinants of the membrane height around the protein. The membrane thins to expose these nitrogens to the high dielectric environment of the headgroup region, in agreement with our simulations and previous work (16). We observe the indole nitrogen creating transient hydrogen bonds with the headgroup phosphate or backbone carbonyls of the adjacent lipids, whereas the tryptophan ring interacts with the positively charged choline through cation-π interactions.

Elasticity equations require two boundary conditions, and here we impose membrane height and membrane slope conditions. Earlier gramicidin studies that used similar boundary conditions found that it was necessary to impose a zero slope on the surface to match experimental results (18,25,31), and later studies with shell hardening revealed that a zero slope condition was no longer needed to match experiment (27). Here, we optimized for the slope that minimizes the total energy, and we found that the most favorable contact slope is moderately positive (but not equal to zero) with a slight variability along the boundary (see Fig. S6).

TRPV1 residues bend the membrane

The numeric advances described here let us explore membrane distortions around embedded proteins with complex shapes, and the continuum nature of our model scales well to large systems. Thus, we used our approach to predict the membrane deformations around TRPV1, a large nonselective cation channel with four voltage-sensor-like domains that harbor basic residues buried in the membrane interface. Previously, we used our software APBSmem (https://apbsmem.sourceforge.io/) to scan through all multipass membrane proteins of known structure and calculate the electrostatic energy (G^e) associated with embedding the protein in a flat, low-dielectric lipidlike environment (40). We found that the closed, capsaicin-bound (partially open), and RTX-bound (fully open) structures returned >10 residues that incurred large electrostatic penalties for being in or near the membrane (Fig. 5 *A*). Examination of the structures revealed that many of these residues were near the hydrophobic interface, but buried in the membrane according to the hydrophobic thickness estimated by the Orientations of Proteins in the Membrane database (69). We reasoned that minor distortions in the membrane may expose these charged and polar residues to water relieving the electrostatic penalty, and we also hypothesized that these membrane deformations may be coupled to the function of the channel. We used our continuum model (Eq. 1) and searched for the membrane configuration that minimized the total energy of the system. As reasoned, the optimal solution exhibits large deformations around the protein, and these deformations significantly reduce the electrostatic insertion penalty of the high energy residues (Fig. 5, *B* and *C*). The membrane deformation energies induced by the closed, partially open, and fully open structures are 38, 52, and 64 kcal/mol, respectively. These energies indicate that as the TRPV1 channel opens, it generates larger membrane deformations. K464 and R491 are two membrane-anchoring residues that are partially responsible for these deformations. In an undeformed membrane, K464 and R491 cause very large 12.8 and 19.9 kcal/mol electrostatic penalties in the open structure, respectively, but these penalties are almost completely relieved when the membrane is allowed to bend. It is tempting to speculate that these residues are involved in thermosensitivity or voltage sensing, and their displacement may bias the

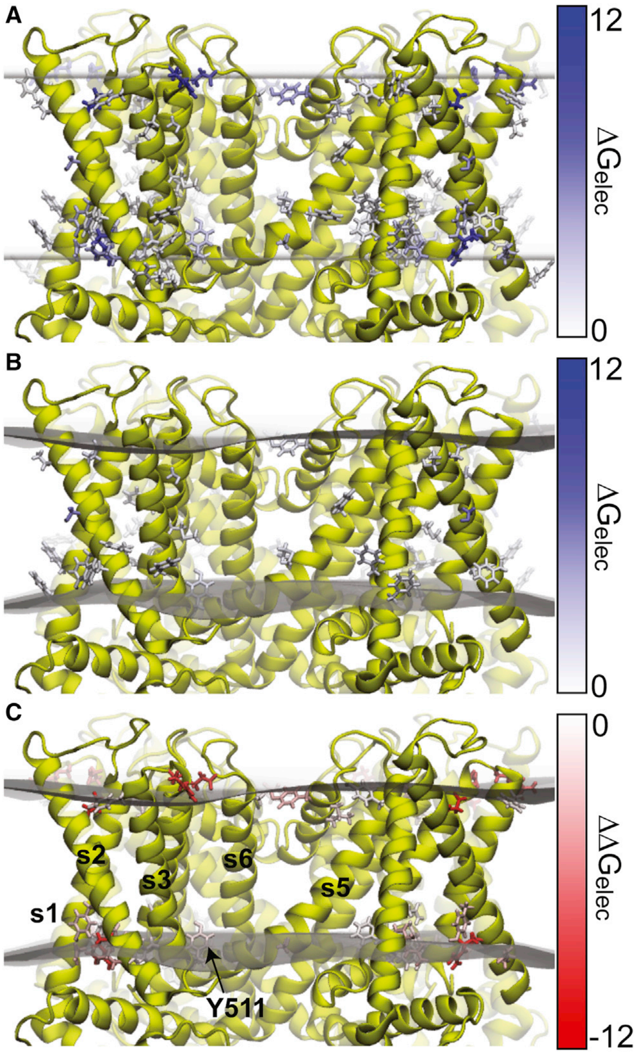

FIGURE 5 The hybrid continuum-atomistic model predicts that TRPV1 deforms the membrane. (*A*) Shown here are the electrostatic membrane insertion penalties for membrane-exposed residues when the membrane is represented as a rigid slab. Hydrophobic interfaces are shown as transparent surfaces. Residues are colored by electrostatic insertion penalty. We calculate this penalty as the electrostatic energy of the protein in membrane minus the electrostatic energy of the protein in solution. (*B*) Electrostatic insertion penalty after the membrane is allowed to deform. In (*A*) and (*B*), only residues with a penalty >1 kcal/mol are shown. (*C*) Given here is the reduction in electrostatic penalty after the membrane is allowed to deform. This is the penalty of (*A*) subtracted from the penalty in (*B*). For clarity, only residues with reductions >1 kcal/mol are shown. Tyr-511 and TM helices are labeled. To see this figure in color, go online.

opening of the channel. However, more detailed experimental analysis on the mechanistic role of K464 and R591 is required.

CONCLUSIONS

Although continuum elasticity theory has been successful at reproducing the long-wavelength equilibrium shapes of membrane structures (41), whether such models can accurately describe membrane deformations at the Ångström length scale has been debated. A 2013 comparison to fully atomistic MD simulations suggests that continuum models fail to reproduce key features observed in the simulations (18). Here, we presented a self-consistent continuum approach to model protein-mediated distortions in the bilayer, which overcomes much of the shortcomings of simpler continuum treatments. Our model builds off of our earlier work in which we accurately represent the protein at the atomic level and incorporates a biophysically meaningful energy model of the system that includes electrostatic, nonpolar, and membrane elastic energies (19,32,38). Here, we have significantly advanced our geometric handling of the protein shape and elasticity calculations by employing a finite volume solver (39) to address insertions of arbitrary shape. The membrane calculations are performed in a distorted grid that is mapped to the membrane-protein boundary, which increases the fidelity of our solver with lower grid densities than a strictly Cartesian grid. We show that the method matches results from MD simulations with high accuracy, and our approach highlights how the boundary conditions of the elastic solver preserve the chemical information of the protein. Nonetheless, the method is computationally fast because it relies on implicit energy models at all stages. Thus, we assert that continuum membrane models have the potential to provide deep insight into membrane-protein interactions involved in a wide range of biological phenomena with high spatial resolution, but with minimal computational overhead.

We validate our continuum model by comparing to MD simulations of gramicidin in a POPC membrane. First, we test our continuum membrane description by only using our elastic solver and boundary conditions extracted from MD. As seen in Fig. 2, the continuum predictions nicely match MD membrane deformation profiles and the extent of the membrane compression ring around gramicidin. We then move on to make predictions for gramicidin orientation and depth of penetration using the full energy model given by Eq. 1 without any input from MD. Our continuum model agrees with the atomistic predictions for membrane contact heights and tilt as shown in Figs. 3 and 4. We show that a flat-slab representation of the membrane fails to determine the preferred protein orientation, indicating that membrane deformation plays a crucial role in determining the final equilibrium configuration. Finally, as an application of our self-consistent continuum model, we study POPC membrane deformations induced by the transient receptor potential cation channel TRPV1. We found that allowing the membrane to deform greatly reduces the electrostatic penalty of charged residues near the headgroup-tail interfaces of the membrane. Our calculations further showed that TRPV1-charged residues generate much larger deformations in the open and partially open structures than the closed structure. Based on this observation, we speculate that the same residues involved in the membrane distortions could be involved in thermosensitivity or voltage sensing. More detailed experimental analysis is required to uncover the mechanistic role of these residues.

When comparing to continuum descriptions of the membrane, the MD surface profiles require careful analysis of periodic boundary effects (32,68) and spatial fluctuations of the protein orientation and side-chain movements. Our MD simulations of the gramicidin channel in a 100 × 100 Å^2 patch reveal that the membrane is not fully relaxed at the edges (Fig. 2). If one desires to match MD simulation results, continuum elastic membrane models should explicitly impose similar far-field conditions. Although gramicidin has been a test case for exploring continuum models of the membrane and comparing these solutions to MD, we believe that it is likely one of the harder systems to match due to the small size of the protein, which allows it to change its orientation in the membrane on a fast timescale resulting in sizable fluctuations in the protein-membrane contours (Fig. 4). Care must be taken when averaging the membrane surfaces from the MD simulations to avoid unphysical artifacts (see Supporting Material), and our experience suggests that comparison between MD and our continuum model is much easier for larger proteins that are better anchored in the membrane (3). Additionally, the computational demand is significantly lower for continuum calculations as opposed to MD. For gramicidin, the boundary conditions and energies can be calculated within 3 h on a desktop CPU, whereas the converged MD surfaces required 54 days of computation time using GPU-accelerated NAMD with 1 GPU and 32 CPUs.

Elastic moduli are key elements of the model that directly impact the membrane deformation energy and surface profiles. Previous work has suggested that these moduli vary spatially due to protein effects (18,27), and we found that including a lipid hardening factor as suggested in Partenskii and Jordan (27) significantly improves the quantitative match between continuum results and atomistic MD. As membrane elastic models become increasingly more sophisticated through the inclusion of spatially dependent elastic moduli that vary with membrane composition (60), we believe that our solver can serve as an efficient tool to test models and elastic constants by quickly calculating energetics and membrane shapes to compare with experiments (23,25,70) and atomistic simulations. Additional experimental estimates of the energetics of the gramicidin-POPC system would be needed to further parameterize continuum models. Lastly, we point out that whereas hardening is a compelling candidate to explain differences between continuum predictions and MD, certainly there are other factors that are known to affect membrane energetics such as lipid tilt (71), entropic cost of lipid confinement (72,73), line tension effects on lipid ordering (74–76), and additional terms penalizing the changes in area per lipid molecule (77). In future work, we plan to refine our elastic model by adding these elements.

Our hybrid continuum-atomistic model offers a distinct advantage over fully atomistic simulations for studying protein-membrane interactions due to its speed and accuracy, and this advantage grows with the size of the system. Because the model accurately reproduces results from MD simulations, we now plan to use it to probe larger, more complex biological situations such as multiprotein problems like the F-ATPase complexes that form rows of proteins along the inner membrane of the mitochondrial cristae (13), M2 channel-mediated fission (78), and SNARE-mediated fusion (79). Because continuum calculations are inexpensive and fast, our model provides a promising framework for exploring these multiprotein phenomena, where we can not only address geometrical effects in the membrane and the protein shape (34,35,37), but also extract membrane deformation energy values and reveal how specific protein structure and chemistry drives the processes.

SUPPORTING MATERIAL

Supporting Materials and Methods and eight figures are available at http://www.biophysj.org/biophysj/supplemental/S0006-3495(17)30394-6.

AUTHOR CONTRIBUTIONS

D.A. designed research, performed research, analyzed data, and wrote the paper. N.P.B. designed research, performed research, analyzed data, and wrote the paper. F.V.M. performed research and analyzed data. C.W.W. contributed numerical tools. M.G. designed research, analyzed data, and wrote the paper.

ACKNOWLEDGMENTS

This work was supported by National Institutes of Health (NIH) grant No. R01-GM117593 and National Science Foundation (NSF) CAREER Award No. MCB-0845286. Computations were performed, in part, at the Texas Advanced Computing Center through the support of grant No. MCB-80011 and the Extreme Science and Engineering Discovery Environment (XSEDE) and the University of California San Francisco.

SUPPORTING CITATIONS

References (80–90) appear in the Supporting Material.

REFERENCES

1. Zimmerberg, J., and M. M. Kozlov. 2006. How proteins produce cellular membrane curvature. *Nat. Rev. Mol. Cell Biol.* 7:9–19.
2. Andersen, O. S., R. E. Koeppe, 2nd, and E. Koeppe. 2007. Bilayer thickness and membrane protein function: an energetic perspective. *Annu. Rev. Biophys. Biomol. Struct.* 36:107–130.
3. Argudo, D., N. P. Bethel, ..., M. Grabe. 2016. Continuum descriptions of membranes and their interaction with proteins: towards chemically accurate models. *Biochim. Biophys. Acta.* 1858:1619–1634.
4. Urry, D. W. 1971. The gramicidin A transmembrane channel: a proposed pi(L,D) helix. *Proc. Natl. Acad. Sci. USA.* 68:672–676.
5. Perozo, E., D. M. Cortes, ..., B. Martinac. 2002. Open channel structure of MscL and the gating mechanism of mechanosensitive channels. *Nature.* 418:942–948.

6. Quemeneur, F., J. K. Sigurdsson, …, D. Lacoste. 2014. Shape matters in protein mobility within membranes. *Proc. Natl. Acad. Sci. USA.* 111:5083–5087.
7. Keller, S. L., S. M. Bezrukov, …, V. A. Parsegian. 1993. Probability of alamethicin conductance states varies with nonlamellar tendency of bilayer phospholipids. *Biophys. J.* 65:23–27.
8. Tonnesen, A., S. M. Christensen, …, D. Stamou. 2014. Geometrical membrane curvature as an allosteric regulator of membrane protein structure and function. *Biophys. J.* 106:201–209.
9. Shibata, Y., J. Hu, …, T. A. Rapoport. 2009. Mechanisms shaping the membranes of cellular organelles. *Annu. Rev. Cell Dev. Biol.* 25:329–354.
10. Cogliati, S., J. A. Enriquez, and L. Scorrano. 2015. Architecture and function of mechanosensitive membrane protein lattices. *Trends in Biomedical Sciences.* 41:261–273.
11. Aridor, M., S. I. Bannykh, …, W. E. Balch. 1995. Sequential coupling between COPII and COPI vesicle coats in endoplasmic reticulum to Golgi transport. *J. Cell Biol.* 131:875–893.
12. Orso, G., D. Pendin, …, A. Daga. 2009. Homotypic fusion of ER membranes requires the dynamin-like GTPase atlastin. *Nature.* 460:978–983.
13. Davies, K. M., C. Anselmi, …, W. Kühlbrandt. 2012. Structure of the yeast F1Fo-ATP synthase dimer and its role in shaping the mitochondrial cristae. *Proc. Natl. Acad. Sci. USA.* 109:13602–13607.
14. Jiko, C., K. M. Davies, …, C. Gerle. 2015. Bovine F1Fo ATP synthase monomers bend the lipid bilayer in 2D membrane crystals. *eLife.* 4:e06119.
15. Ambroso, M. R., B. G. Hegde, and R. Langen. 2014. Endophilin A1 induces different membrane shapes using a conformational switch that is regulated by phosphorylation. *Proc. Natl. Acad. Sci. USA.* 111:6982–6987.
16. Kim, T., K. I. Lee, …, W. Im. 2012. Influence of hydrophobic mismatch on structures and dynamics of gramicidin a and lipid bilayers. *Biophys. J.* 102:1551–1560.
17. Yoo, J., and Q. Cui. 2013. Membrane-mediated protein-protein interactions and connection to elastic models: a coarse-grained simulation analysis of gramicidin A association. *Biophys. J.* 104:128–138.
18. Lee, K. I., R. W. Pastor, …, W. Im. 2013. Assessing smectic liquid-crystal continuum models for elastic bilayer deformations. *Chem. Phys. Lipids.* 169:19–26.
19. Choe, S., K. A. Hecht, and M. Grabe. 2008. A continuum method for determining membrane protein insertion energies and the problem of charged residues. *J. Gen. Physiol.* 131:563–573.
20. Mondal, S., G. Khelashvili, …, H. Weinstein. 2011. Quantitative modeling of membrane deformations by multihelical membrane proteins: application to G-protein coupled receptors. *Biophys. J.* 101:2092–2101.
21. Ollila, O. H. S., H. J. Risselada, …, S. J. Marrink. 2009. 3D pressure field in lipid membranes and membrane-protein complexes. *Phys. Rev. Lett.* 102:078101.
22. Yoo, J., and Q. Cui. 2013. Three-dimensional stress field around a membrane protein: atomistic and coarse-grained simulation analysis of gramicidin A. *Biophys. J.* 104:117–127.
23. Huang, H. W. 1986. Deformation free energy of bilayer membrane and its effect on gramicidin channel lifetime. *Biophys. J.* 50:1061–1070.
24. Ring, A. 1996. Gramicidin channel-induced lipid membrane deformation energy: influence of chain length and boundary conditions. *Biochim. Biophys. Acta.* 1278:147–159.
25. Nielsen, C., M. Goulian, and O. S. Andersen. 1998. Energetics of inclusion-induced bilayer deformations. *Biophys. J.* 74:1966–1983.
26. Harroun, T. A., W. T. Heller, …, H. W. Huang. 1999. Theoretical analysis of hydrophobic matching and membrane-mediated interactions in lipid bilayers containing gramicidin. *Biophys. J.* 76:3176–3185.
27. Partenskii, M. B., and P. C. Jordan. 2002. Membrane deformation and the elastic energy of insertion: perturbation of membrane elastic constants due to peptide insertion. *J. Chem. Phys.* 117:10768–10776.
28. Harroun, T. A., W. T. Heller, …, H. W. Huang. 1999. Experimental evidence for hydrophobic matching and membrane-mediated interactions in lipid bilayers containing gramicidin. *Biophys. J.* 76:937–945.
29. May, S. 2000. Theories on structural perturbations of lipid bilayers. *Curr. Opin. Colloid Interface Sci.* 5:244–249.
30. Helfrich, P., and E. Jakobsson. 1990. Calculation of deformation energies and conformations in lipid membranes containing gramicidin channels. *Biophys. J.* 57:1075–1084.
31. Nielsen, C., and O. S. Andersen. 2000. Inclusion-induced bilayer deformations: effects of monolayer equilibrium curvature. *Biophys. J.* 79:2583–2604.
32. Latorraca, N. R., K. M. Callenberg, …, M. Grabe. 2014. Continuum approaches to understanding ion and peptide interactions with the membrane. *J. Membr. Biol.* 247:395–408.
33. Panahi, A., and M. Feig. 2013. Dynamic heterogeneous dielectric generalized born (DHDGB): an implicit membrane model with a dynamically varying bilayer thickness. *J. Chem. Theory Comput.* 9:1709–1719.
34. Haselwandter, C. A., and R. Phillips. 2013. Connection between oligomeric state and gating characteristics of mechanosensitive ion channels. *PLOS Comput. Biol.* 9:e1003055.
35. Kahraman, O., P. D. Koch, …, C. A. Haselwandter. 2016. Architecture and function of mechanosensitive membrane protein lattices. *Sci. Rep.* 6:19214.
36. Mondal, S., G. Khelashvili, …, H. Weinstein. 2013. The cost of living in the membrane: a case study of hydrophobic mismatch for the multi-segment protein LeuT. *Chem. Phys. Lipids.* 169:27–38.
37. Haselwandter, C. A., and R. Phillips. 2013. Directional interactions and cooperativity between mechanosensitive membrane proteins. *Europhys. Lett.* 101:1–6.
38. Callenberg, K. M., N. R. Latorraca, and M. Grabe. 2012. Membrane bending is critical for the stability of voltage sensor segments in the membrane. *J. Gen. Physiol.* 140:55–68.
39. Wolgemuth, C. W., and M. Zajac. 2010. The moving boundary node method: a level set-based, finite volume algorithm with applications to cell motility. *J. Comput. Phys.* 229:7287–7308.
40. Marcoline, F. V., N. Bethel, …, M. Grabe. 2015. Membrane protein properties revealed through data-rich electrostatics calculations. *Structure.* 23:1526–1537.
41. Deserno, M. 2015. Fluid lipid membranes: from differential geometry to curvature stresses. *Chem. Phys. Lipids.* 185:11–45.
42. Fošnarič, M., A. Iglič, and S. May. 2006. Influence of rigid inclusions on the bending elasticity of a lipid membrane. *Phys. Rev. E Stat. Nonlin. Soft Matter Phys.* 74:051503.
43. Bingham, R. J., P. D. Olmsted, and S. W. Smye. 2010. Undulation instability in a bilayer lipid membrane due to electric field interaction with lipid dipoles. *Phys. Rev. E Stat. Nonlin. Soft Matter Phys.* 81:051909.
44. Watson, M. C., E. S. Penev, …, F. L. H. Brown. 2011. Thermal fluctuations in shape, thickness, and molecular orientation in lipid bilayers. *J. Chem. Phys.* 135:244701.
45. Watson, M. C., A. Morriss-Andrews, …, F. L. H. Brown. 2013. Thermal fluctuations in shape, thickness, and molecular orientation in lipid bilayers. II. Finite surface tensions. *J. Chem. Phys.* 139:084706.
46. Kamien, R. D. 2002. The geometry of soft materials: a primer. *Rev. Mod. Phys.* 74:953–971.
47. Brannigan, G., and F. L. H. Brown. 2007. Contributions of Gaussian curvature and nonconstant lipid volume to protein deformation of lipid bilayers. *Biophys. J.* 92:864–876.
48. Callenberg, K. M. 2013. Membrane bending is critical for assessing the thermodynamic stability of proteins in the membrane. Ph.D. thesis, University of Pittsburgh, Pittsburgh, PA.
49. Powell, M. 1964. An efficient method for finding the minimum of a function of several variables without calculating derivatives. *Comput. J.* 7:155–162.

50. Nelder, J., and R. Mead. 1965. A simplex method for function minimization. *Comput. J.* 7:308–313.
51. Richards, F. M. 1977. Areas, volumes, packing and protein structure. *Annu. Rev. Biophys. Bioeng.* 6:151–176.
52. Hardt, R., D. Kinderlehrer, and F.-H. Lin. 1986. Existence and partial regularity of static liquid crystal configurations. *Commun. Math. Phys.* 105:547–570.
53. Stewart, I. W. 2004. The Static and Dynamic Continuum Theory of Liquid Crystals. Taylor and Francis, London, UK.
54. Hu, M., J. J. Briguglio, and M. Deserno. 2012. Determining the Gaussian curvature modulus of lipid membranes in simulations. *Biophys. J.* 102:1403–1410.
55. Hu, M., D. H. de Jong, …, M. Deserno. 2013. Gaussian curvature elasticity determined from global shape transformations and local stress distributions: a comparative study using the MARTINI model. *Faraday Discuss.* 161:365–382.
56. Helfrich, W. 1994. Lyotropic lamellar phases. *J. Phys. Condens. Matter.* 6:A79–A92.
57. Dimova, R. 2014. Recent developments in the field of bending rigidity measurements on membranes. *Adv. Colloid Interface Sci.* 208:225–234.
58. Nagle, J. F., M. S. Jablin, …, K. Akabori. 2015. What are the true values of the bending modulus of simple lipid bilayers? *Chem. Phys. Lipids.* 185:3–10.
59. Levine, Z. A., R. M. Venable, …, F. L. H. Brown. 2014. Determination of biomembrane bending moduli in fully atomistic simulations. *J. Am. Chem. Soc.* 136:13582–13585.
60. Venable, R. M., F. L. H. Brown, and R. W. Pastor. 2015. Mechanical properties of lipid bilayers from molecular dynamics simulation. *Chem. Phys. Lipids.* 192:60–74.
61. Townsley, L. E., W. A. Tucker, S. Sham, and J. F. Hinton. 2001. Structures of gramicidins A, B, and C incorporated into sodium dodecyl sulfate micelles. *Biochemistry.* 40:11676–11686.
62. Lee, J., X. Cheng, …, W. Im. 2016. CHARMM-GUI input generator for NAMD, GROMACS, AMBER, OpenMM, and CHARMM/OpenMM simulations using the CHARMM36 additive force field. *J. Chem. Theory Comput.* 12:405–413.
63. Jorgensen, W. L., J. Chandrasekhar, …, M. L. Klein. 1983. Comparison of simple potential functions for simulating liquid water. *J. Chem. Phys.* 79:926–935.
64. Phillips, J. C., R. Braun, …, K. Schulten. 2005. Scalable molecular dynamics with NAMD. *J. Comput. Chem.* 26:1781–1802.
65. Klauda, J. B., R. M. Venable, …, R. W. Pastor. 2010. Update of the CHARMM all-atom additive force field for lipids: validation on six lipid types. *J. Phys. Chem. B.* 114:7830–7843.
66. de Planque, M. R. R., and J. A. Killian. 2003. Protein-lipid interactions studied with designed transmembrane peptides: role of hydrophobic matching and interfacial anchoring. *Mol. Membr. Biol.* 20:271–284.
67. Goulian, M., O. N. Mesquita, …, A. Libchaber. 1998. Gramicidin channel kinetics under tension. *Biophys. J.* 74:328–337.
68. Hu, Y., S. Ou, and S. Patel. 2013. Free energetics of arginine permeation into model DMPC lipid bilayers: coupling of effective counterion concentration and lateral bilayer dimensions. *J. Phys. Chem. B.* 117:11641–11653.
69. Lomize, M. A., A. L. Lomize, …, H. I. Mosberg. 2006. OPM: orientations of proteins in membranes database. *Bioinformatics.* 22:623–625.
70. Elliott, J., D. Needham, …, D. Haydon. 1983. The effects of bilayer thickness and tension on gramicidin single-channel lifetime. *Biochim. Biophys. Acta.* 735:95–103.
71. Hamm, M., and M. M. Kozlov. 2000. Elastic energy of tilt and bending of fluid membranes. *Eur. Phys. J. E.* 3:323–335.
72. May, S. 2002. Membrane perturbations induced by integral proteins: the role of conformational restrictions of the lipid chains. *Langmuir.* 18:6356–6364.
73. Bohinc, K., V. Kralj-Iglič, and S. May. 2003. Interaction between two cylindrical inclusions in a symmetric lipid bilayer. *J. Chem. Phys.* 119:7435–7444.
74. Kuzmin, P. I., S. A. Akimov, …, F. S. Cohen. 2005. Line tension and interaction energies of membrane rafts calculated from lipid splay and tilt. *Biophys. J.* 88:1120–1133.
75. García-Sáez, A. J., S. Chiantia, and P. Schwille. 2007. Effect of line tension on the lateral organization of lipid membranes. *J. Biol. Chem.* 282:33537–33544.
76. Katira, S., K. K. Mandadapu, …, D. Chandler. 2016. Pre-transition effects mediate forces of assembly between transmembrane proteins. *eLife.* 5:e13150.
77. Bitbol, A. F., D. Constantin, and J.-B. Fournier. 2012. Bilayer elasticity at the nanoscale: the need for new terms. *PLoS One.* 7:e48306.
78. Rossman, J. S., X. Jing, …, R. A. Lamb. 2010. Influenza virus M2 protein mediates ESCRT-independent membrane scission. *Cell.* 142:902–913.
79. Weber, T., B. V. Zemelman, …, J. E. Rothman. 1998. SNAREpins: minimal machinery for membrane fusion. *Cell.* 92:759–772.
80. Sharp, K. A., and B. Honig. 1990. Electrostatic interactions in macromolecules: theory and applications. *Annu. Rev. Biophys. Biophys. Chem.* 19:301–332.
81. Baker, N. A., D. Sept, …, J. A. McCammon. 2001. Electrostatics of nanosystems: application to microtubules and the ribosome. *Proc. Natl. Acad. Sci. USA.* 98:10037–10041.
82. Sanner, M. F., A. J. Olson, and J.-C. Spehner. 1996. Reduced surface: an efficient way to compute molecular surfaces. *Biopolymers.* 38:305–320.
83. Sitkoff, D., N. Ben-Tal, and B. Honig. 1996. Calculation of alkane to water solvation free energies using continuum solvent models. *J. Phys. Chem.* 100:2744–2752.
84. Fournier, J.-B. 1999. Microscopic membrane elasticity and interactions among membrane inclusions: interplay between the shape, dilation, tilt and tilt-difference modes. *Eur. Phys. J. B Cond. Matter Complex Syst.* 11:261–272.
85. Schmid, F. 2011. Are stress-free membranes really “tensionless”? *EPL.* 95:28008.
86. Diamant, H. 2011. Model-free thermodynamics of fluid vesicles. *Phys. Rev. E Stat. Nonlin. Soft Matter Phys.* 84:061123.
87. Safran, A. S. 2003. Statistical Thermodynamics of Surfaces, Interfaces, and Membranes. Frontiers in Physics. Westview Press, Boulder, CO.
88. Boal, D. 2012. Mechanics of the Cell,, 2nd. Cambridge University Press, Cambridge, UK.
89. Aranda-Espinoza, H., A. Berman, …, S. Safran. 1996. Interaction between inclusions embedded in membranes. *Biophys. J.* 71:648–656.
90. Bolza, O. 1961. Lectures on the Calculus of Variations. Dover Publications, Mineola, NY.
91. Sitkoff, D., K. A. Sharp, and B. Honig. 1994. Accurate calculation of hydration free energies using macroscopic solvent models. *J. Phys. Chem.* 98:1978–1988.

Biophysical Journal, Volume *112*

Supplemental Information

New Continuum Approaches for Determining Protein-Induced Membrane Deformations

David Argudo, Neville P. Bethel, Frank V. Marcoline, Charles W. Wolgemuth, and Michael Grabe

Supporting Material: New continuum approaches for determining protein induced membrane deformations

David Argudo[*], Neville P. Bethel[*], Frank V. Marcoline[*], Charles W. Wolgemuth[‡] and Michael Grabe[*]

∗ *Cardiovascular Research Institute, Department of Pharmaceutical Chemistry, University of California San Francisco, San Francisco, CA 94158, USA.*

‡ *Departments of Molecular and Cellular Biology and Physics, University of Arizona, Tucson, Arizona.*

S1. Analysis of molecular dynamics membrane deformation profiles: effects at the boundaries

To compare molecular dynamics (MD) simulation results with our continuum-atomistic model, we averaged lipid positions of individual MD snapshots to obtain a final equilibrium membrane shape. The procedure is described in *Simulation Methods* in the main text. Fig. S1 shows the running time average of the membrane thickness, which indicates the time required to average out spatial fluctuations to arrive at a converged static pattern. Panel (A) contains a gramicidin dimer and (B) is a protein free bilayer. Analysis of these profiles reveals several interesting features. First, even at 100 ns, the protein free system exhibits a spatial pattern showing inhomogeneity present in the starting configuration. The magnitude of the inhomogeneity is much reduced (10 Å at 25 ns versus 4 Å at 100 ns), and it is centered on the bulk equilibrium thickness of 28.5 Å, but a pattern persists nonetheless. The pinching pattern in the gramicidin simulations is set up quickly (in 25 ns), but the spatial fluctuations are so large that the system must be averaged for at least 250 ns before a somewhat static pattern emerges. This time difference when compared to the protein-free system is not surprising since the membranes are pre-equilibrated in a flat undeformed state closer to the protein-free simulation. But we want to point out that even these simple simulations must be averaged for 200 ns, preferably more (500 ns in the main text), to achieve static patterns. Second, protein induced deformations extend to the simulation boundaries indicating that bilayer patch size should be carefully considered to allow full relaxation to bulk values at the boundaries. At 250 ns, panel (A) shows the membrane height reaches bulk values (28.5 Å) at the corners of the periodic box (55 Å from the center), but not at the centers of each side (40 Å from the center). If the box is too small, periodic boundary conditions will muddy interpretation of the patterns.

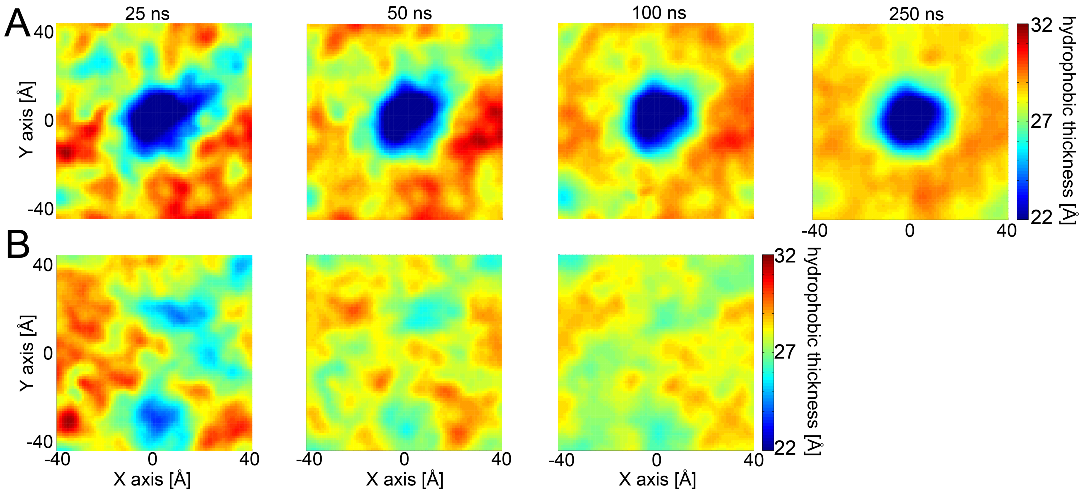

Figure S1: Running time average of hydrophobic mismatch from MD simulations with gramicidin (A) and without protein (B). Both systems contain POPC lipids. In panel A, membrane height values converge to the bulk value (~28.5 Å) at the corners of the simulation box between 100 ns and 250 ns, but the pattern is still fluctuating when averaged for less time. Moreover, at the center of the outer edges of the box (40 Å from the protein) the membrane heights are 2-3 Å higher than bulk values. (B) MD simulation of a pure POPC membrane. Even after averaging for 100 ns a spatial pattern persists, but the amplitude of the fluctuations is only ±2 Å from the mean value of 28.5 Å.

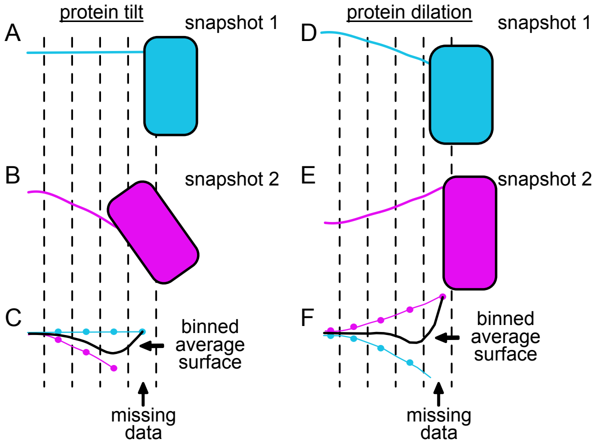

Figure S2: Averaging membrane configurations can produce unrealistic surfaces. (A-B) Binning a straight (A) and tilted (B) protein configuration. When the protein tilts to the left, the protein-membrane boundary also shifts to the left. (C) Combining bins from configurations A and B leads to non-monotonic behavior that is otherwise not present in either configuration. (D-E) Binning membrane surfaces from snapshots in which the protein radius is dilated (D) or constricted (E). The later configuration is representative of what occurs during the creation of *hotspots* in which individual lipid molecules extend over the top of the channel to interact with specific tryptophan residues. (F) Combining bins from configurations D and E leads to non-monotonic behavior, which is not representative of either configuration.

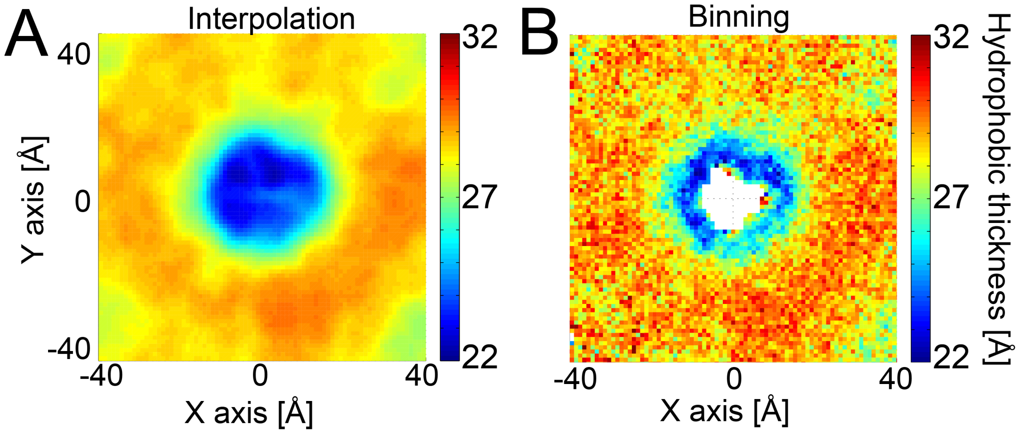

Figure S3: Different averaging methods produce different membrane hydrophobic thickness profiles. (A) Surface profile obtained using an interpolation averaging method. For each snapshot, membrane heights are first interpolate to a two dimensional grid of one Å spacing. All grid points are evaluated regardless of protein occupancy. The final surface is the average of all grids over the course of the trajectory. We see that extending radially away from the center of the membrane, the deformation profile exhibits pure monotonic behavior (blue to red) within a distance comparable to the width of a few lipid shells. (B) Surface profile obtained using a bin-based averaging method that simply averages local lipid height in each snapshot (each bin is 1 Å^2). Unlike the method in panel (A), if a lipid is not located within a bin for a given snapshot, the bin will receive no value. For bins near the protein boundary, they are often occupied by protein, and hence rarely populated by lipid. There are several localized *hotspots* adjacent to the protein where the membrane becomes very thick, 32 Å. Extending radially away from the protein in these regions, the membrane deformation profile exhibits non-monotonic behavior within a distance comparable to the width of a few lipid shells. The simulation system is composed of POPC lipids and the protein is gramacidin. For both methods, the protein was centered from snapshot to snapshot prior to computing membrane heights.

We carefully considered several methods for averaging the surfaces from MD, because the average of a solution set often results in an entity that is not a member of the set. However, averaged membrane surface profiles should reflect, as much as possible, an equilibrium membrane distortions that is physically allowable. Gramicidin is a small peptide and during MD simulations the protein position and tilt orientation fluctuate resulting in corresponding fluctuations in the protein-membrane boundary. If these changes are not carefully accounted for during averaging, it can magnify artifacts resulting from averaging. One option for averaging involves binning membrane height at the upper and lower leaflets to determine the thickness profile. To do this, we created a 2D grid of squares 1 Å in size, one for the upper surface and one for the lower surface, and recorded the heights of upper/lower lipid molecules in each respective bin for every snapshot. However, as shown in Fig S2 this approach leads to two scenarios that produce artifacts when binning results from MD. Panels (A-C) show the effect of binning straight (A) and tilted (B) protein configurations. Panel (C) shows how the tilted configuration in (B) results in missing data, and combining bins from configurations (A) and (B) leads to non-mononotic behavior that is otherwise not present in either true configuration. Similarly panels (D-F) show the effect of binning a protein with a dilated effective radius (D) at one point in time and constricted effective radius (B) at another. The averaged surface in (F) has missing data resulting from configuration (D), and it also exhibits non-monotonic behavior. This later scenario occurs during the creation of *hotspots* in which individual lipid molecules extend over the top of the channel to interact with specific tryptophan residues (1). When *hotspots* are present, the effective protein area is reduced due to lipids encroach on the protein-occupied region. Panel (F) shows how combining bins from both configurations leads to non-mononotic behavior that is otherwise not present in (D) or (E).

As an alternative approach to determining representative, averages of the membrane surface, we used an interpolation procedure where each node value of a Cartesian grid was assigned the interpolated z-value of nearby lipid C2 carbon atoms for each MD snapshot. This approach guarantees that every node of the surface has a value for each membrane configuration. Fig. S3 shows a comparison between the membrane thickness obtained using the interpolation (A) and binning (B) methods. In the interpolation averaging procedure (A) the membrane deformation profile that extends radially away from the protein exhibits a monotonic behavior (blue to red) within a distance comparable to the width of a few lipid shells, while the binning method (B) generates a non-monotonic radial profile arising from *hotspots* near the protein (red and yellow) with increased thickness. Analysis of the specific MD snapshots that give rise to the non-monotonic behavior in the averaged surfaces in Fig. S3 B are themselves radially monotonic near the protein indicating that the averaged thickness profile harbors artifacts likely resulting from the mechanisms illustrated in Fig. S2. Moreover, the non-monotonic profile is highly curved with a high corresponding deformation energy casting further doubts on the physical appropriateness of the binning scheme. A deeper analysis of the influence *hotspots* (black or white circled region) play on the binned hydrophobic profile (reproduced in Fig. S4 A) shows that they are poorly sampled bins (panel B), yet they dramatically influence the final average thickness. We computed the membrane thickness with this sparse data corresponding to only membrane configurations in which the textithotspot was populated, and the resulting average profile is radially monotonic within the first few lipid shells (panel (C)). Importantly, the membrane is quite thick for these snapshots, but the radial relaxation is smooth. We conclude that individual membrane configurations are quite smooth in the first few lipid shells adjacent to the protein, and simple binning schemes mask this observation.

S2. Non-Elastic Energy terms

S2.1. Electrostatic Energy $G^{(e)}$

The electrostatic energy of the inclusion in the bilayer was determined using the non-linear Poisson-Boltzmann equation (in e.s.u-c.g.s unit system) (2, 3):

$$-\nabla \cdot [\epsilon(\vec{p})\nabla\phi(\vec{p})] + \epsilon(\vec{p})\kappa^2(\vec{p})\sinh[\phi(\vec{p})] = \frac{e}{k_{\mathrm{B}}T}4\pi\rho(\vec{p}), \quad \phi(\vec{p}) = \frac{e\Phi(\vec{p})}{k_{\mathrm{B}}T}, \tag{S1}$$

where $\phi(\vec{p})$ is the reduced electrostatic potential at position $\vec{p}$, k_{B} is the Boltzmann constant, T is the absolute temperature, κ is the Debye-Huckel screening coefficient, ϵ is the spatially-dependent dielectric constant, ρ is the space-dependent charge density within the protein and e is the elementary charge. The electrostatic calculations were carried out using the APBS software (3) together with modifications to include membrane dielectric effects as described in

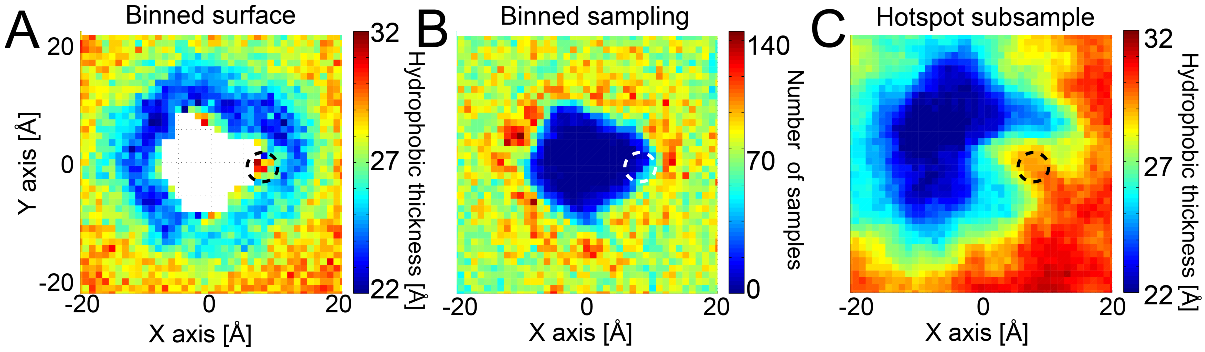

Figure S4: Hotspots are rare, but still smooth. (A) Binned POPC average thickness around gramacidin (same as Fig. S3 B). The dashed oval encompasses a single *hotspot* where lipids extend up over the channel, and the oval corresponds to the region in all three panels. (B) Bin occupancy by lipids during MD simulation. The *hotspot* is rarely sampled by a lipid. (C) Membrane thickness calculated using only snapshots in which a lipid occupies the *hotspot*. The surface was constructed with the interpolation method, since binning resulted in a highly discontinuous surface due to poor sampling. The resulting profile is monotonic and smooth in the radial direction, and these properties are present in the individual snapshots.

Callenberg (4). As in our recent work Ref. (5), a six way flood fill method is used to add the dielectric influence of the membrane to the protein system. Additional details on the electrostatic calculations can be found in our previous publications (5, 6). Finally, we point out that in our calculations we include the effects of ionic screening, but find that the strength of the ionic solution has little effect in the membrane deformations induced by gramicidin. Setting the ionic strength to zero or increasing it by an order of magnitude changes the energy by less than 0.5 kcal/mol.

S2.2. Nonpolar Energy $G^{(np)}$

The non-polar energy of the protein in the membrane environment is related to the amount of protein surface area buried in the membrane. Here, we assume the non-polar energy is:

$$G^{(np)} = a \cdot (A_{mem} - A_{sol}) , \tag{S2}$$

where A_{mem} is the protein's solvent accessible surface area (SASA) in the membrane and A_{sol} is the total SASA in solution. The total protein A_{sol} and per atom surface areas are calculated using Michael Sanner's Molecular Surface program, MSMS (7). To determine A_{men}, membrane exposed atoms were first identified using the same six way flood fill algorithm used for the electrostatic calculations. Atoms that are determined to be membrane exposed are set to have an $A_{mem} = 0.0$. The nonpolar energy of each atom was calculated based on its height relative to the leaflets of the membrane. For atoms in the membrane core, its SASA was multiplied by the surface tension, $a = 0.028$ (kcal/mol)/Å^2. For atoms in the headgroup regions, the surface tension constant decays linearly from 0.028 to 0.00 (kcal/mol)/Å^2 over the 8 Å thickness of the headgroups. The phenomenological constant 0.028 (kcal/mol)/Å^2 is taken from the work of Sitkoff and co-workers (8), and we ignore the constant term usually found in these treatments to zero given that it is typically a small energetic value when compared to other terms in our theory. For more details see Refs. (5, 6).

S2.3. Protein Orientational Entropy $G^{(o)}$

The orientational entropy cost is the energetic penalty associated with the protein's inability to explore certain configurations when inserted in the membrane, which can be expressed in terms of the Euler angles ρ, θ and ϕ describing the protein's orientation in the membrane. The angle ρ represent rotations about the long axis of the protein, θ is the angle created between the z-axis of the membrane and the long axis of the protein (See Fig. 3 in main text), and ϕ represents rotations of the protein about the z-axis of the membrane. As the protein axis tips away from the membrane normal (θ), it is able to explore a greater number of states associated with free rotation about ϕ. The entropy at a given θ value in the range $\delta\theta$ is related to the area swept out by the tip of the protein as it rotates about ϕ. Thus, the entropic energy change with respect to the protein aligned with the membrane normal is given by:

$$G^{(o)} = -k_B T \ln\left(\frac{\Delta A_\theta}{\Delta A_0}\right), \tag{S3}$$

where ΔA_θ is the area swept out by the tip of the helix over the surface of a sphere and ΔA_0 is the effective area explored by the helix tip when it is oriented vertically. The ratio in areas is then given by:

$$\frac{\Delta A_\theta}{\Delta A_0} = \frac{\int_{\theta-\delta\theta}^{\theta+\delta\theta} \sin\theta d\theta}{\int_0^{\delta\theta} \sin\theta d\theta}, \tag{S4}$$

where $\delta\theta \approx r/h$ accounts for tilt angle spanned by a cylinder of finite radius r and height h.

S3. Geometrical description of the membrane

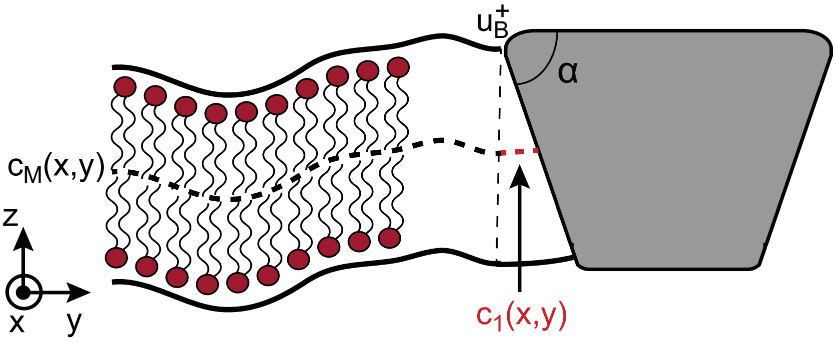

Figure S5: Cartoon model of the membrane in the presence of a conically shaped protein. In the regions where the upper and lower leaflet both exist, the compression surface is labeled $c_M(x, y)$, while in regions where either the upper or lower leaflet does not exist, the compression surface is labeled $c_1(x, y)$. The variable u_B^+ corresponds to the membrane boundary displacements at the interface between the protein and the upper leaflet. The angle α of the conically shaped protein can be used to describe the degree of mismatch between the upper and lower leaflets.

We start by defining the geometry of the system. In Fig. S5, we illustrate a special case where the conical shape of an inclusion causes a mismatch between a region of the upper monolayer and the lower monolayer. A lack of corresponding patch along the z-direction poses a problem for the compression coupling between the leaflets. In general, protein shapes are complex, and this coupling problem arises in many instances. To address this type of biological problems we propose a two-sheet membrane model where the compression of each sheet is derived independently with respect to the bilayer compression surface $c_M(x, y)$ which acts as the coupling element between leaflets (Fig. S5).

We use small deflection theory (9, 10) to model the monolayer surfaces. We define the normal vector to the surface representing the upper monolayer as $\vec{N}^+$ and the lower monolayer as $\vec{N}^-$, which are approximately given by the following relations (9, 11):

$$\vec{N}^+ = \left\{\frac{\partial h^+}{\partial x_1}, \frac{\partial h^+}{\partial x_2}, -1\right\}, \quad \vec{N}^- = -\left\{\frac{\partial h^-}{\partial x_1}, \frac{\partial h^-}{\partial x_2}, -1\right\}. \tag{S5}$$

The variables $h^\pm(x_1, x_2)$ represent the shape, or distance from $z = 0$, of each leaflet. From the shape variables, we define the normalized variables $u^\pm(x_1, x_2)$ as the difference between the shape function of the upper and lower monolayer $h^\pm(x_1, x_2)$ with respect to the flat, undistorted monolayer thickness h_0:

$$u^\pm(x_1, x_2) = h^\pm(x_1, x_2) \mp h_0. \tag{S6}$$

The deformation represented by the leaflet shape variables given in Eq. S6 is equivalent to the mathematical description of bilayer deformation in terms of a dilation variable $d = (u^+ - u^-)/2$ and the bilayer midplane $h = (u^+ + u^-)/2$ (12). Finally, it important to distinguish the true monolayer surface in three dimensional space ($\Gamma^\pm$) from the two dimensional projection of the surface used in calculations ($\Omega^\pm$):

$$d\Gamma^\pm \approx \left[\sqrt{1 + (\nabla u^\pm)^2}\right] d\Omega^\pm \approx \left[1 + \frac{(\nabla u^\pm)^2}{2}\right] dxdy, \tag{S7}$$

where $d\Omega^\pm$ is the differential $dxdy$ in the projected plane (9).

S4. Elastic energy of an arbitrarily shaped inclusion in the membrane

We describe the total elastic energy of the system as the sum of the independent contributions of each monolayer:

$$G^T = E_m^+ + E_m^-, \tag{S8}$$

where +/− denotes variable associated with the upper/lower monolayer, respectively. We account for energies associated with mean curvature bending ($E_B^\pm$), changes in the area per lipid (compression) ($E_C^\pm$), surface tension ($E_S^\pm$), and changes in the gaussian curvature ($E_G^\pm$):

$$E_m^\pm = E_B^\pm + E_S^\pm + E_C^\pm + E_G^\pm, \tag{S9}$$

where each term is briefly described in the following sections.

S4.1. Mean bending curvature

The bending energy is (9):

$$E_B^\pm = \frac{1}{2}\int_{\Gamma^\pm} K_b^\pm \left(2H^\pm + J_0^\pm\right)^2 d\Gamma^\pm, \tag{S10}$$

where the integration is performed over each monoloyer surface $\Gamma^\pm$, $K_b^\pm$ are the monolayer bending moduli, $H^\pm$ are the mean curvature fields describing the neutral surfaces of each monolayer, and $J_0^\pm$ are the spontaneous curvatures in each leaflet. Under small deformations, the mean curvature can be approximated as (9, 13):

$$H^+ = \vec{\nabla}\vec{N}^+ \approx \frac{1}{2}\nabla^2 u^+(x_1, x_2) \quad \text{and} \quad H^- = \vec{\nabla}\vec{N}^- \approx -\frac{1}{2}\nabla^2 u^-(x_1, x_2). \tag{S11}$$

For the chosen normal vectors in Eq. S5 positive curvature H^+ at the upper leaflet is a concave up shape, while positive curvature H^- at the lower leaflet is concave down. The plus sign in front of the spontaneous curvature term $J_0^\pm$ follows the standard convention that a lipid in equilibrium with a positive spontaneous curvature is one with a large headgroup that prefers to adopt a micelle geometry (9). Since this sign convention varies in the literature, care must be taken when comparing different Hamiltonians (9, 10).

Making use of the definitions of the projected area and expanding up to quadratic order in the deformation variables, the bending energy is (9):

$$E_B^\pm \approx \frac{1}{2}\int_{\Omega^\pm} K_b^\pm \left(\nabla^2 u^\pm \pm J_0^\pm\right)^2 + \frac{K_b^\pm}{2}\left(J_0^\pm\right)^2 (\nabla u^\pm)^2 \, dxdy. \tag{S12}$$

S4.2. Surface tension

The tension/stretching energy ($E_S^\pm$) for each monolayer can be written as (9):

$$E_S^\pm = \int_{\Gamma^\pm} \sigma^\pm d\Gamma^\pm - \sigma^\pm \Gamma_0, \tag{S13}$$

where σ is the surface tension parameter, and the integration is performed along the neutral surface of each monoloyer $\Gamma^\pm$. Γ_0 is the initial undeformed area of the membrane, and it is the same for both upper and lower monolayers. Making use of Eq. S7, we can rewrite expression Eq. S13 as:

$$E_S^\pm = \frac{1}{2}\int_{\Omega^\pm} \sigma^\pm (\nabla u^\pm)^2 \, dxdy. \tag{S14}$$

It is important to point out that the surface tension parameter σ is a subtle term that has generated significant controversy depending on its physical interpretation (9). For a detailed description of the numerous interpretations of this term, we refer the reader to the works of Schmid (14), Diamant (15) and Watson et al. (16). Here, we interpret σ to be the conjugate variable that opposes the addition of new area to the total bilayer surface Γ. For constant area per lipid, Γ is proportional to the total number of lipids, and therefore, σ plays the role of the chemical potential. Combining the $\nabla^2 u^\pm$ term in Eq. S12 with Eq. S14, we obtain the effective surface tension parameter $\gamma^\pm = \sigma^\pm + K_B^\pm (J_0^\pm)^2/2$. In the main text, we have expressed the energy in terms of the effective surface tension $\gamma^\pm$.

In addition to the gradient term, $\sigma(\nabla u^\pm)^2$, in the Hamiltonian, it is often common to find a linear term in the literature, $\sigma(u^+ - u^-)$, that arises due to changes in lipid area for a volume incompressible membrane (16–18). This linear term results in systematic change in the equilibrium thickness of the membrane (16, 18):

$$L_0^* = L_0\left(1 - \frac{\sigma}{K_a}\right), \tag{S15}$$

where K_a is the bilayer compression modulus, L_0 is the membrane thickness of a tension-free membrane and L_0^* is the new equilibrium membrane thickness. Using Eq. S15, we can rewrite our deformation variables $u^\pm$ with respect to L_0^* rather than L_0. By doing this change of reference configuration, we recover the same Hamiltonian (without a linear term) in our deformation variables u^+ and u^-. Membrane vesicles are known to burst when the tension goes beyond a few mN/m, but exact values for the surface tension as a function of the membrane composition and protein are unknown. For this reason we have decided to use $\sigma \approx 3$ mN/m as originally postulated by H.W. Huang (13) and often employed in more recent works (6, 19–22). Adding the linear term and keeping $\sigma \approx 3$ mN/m results in a membrane thickness shift $L_0 - L_0^*$ of less than 1.4%.

S4.3. Bilayer compression

As derived in Refs. (17, 23), the compression energy for each monolayer is given by:

$$E_C^\pm \approx \int_{\Omega^\pm} \frac{K_a^\pm}{2}\left(\frac{A^\pm - A_0}{A_0}\right)^2 d\Omega^\pm, \tag{S16}$$

where A_0 is the initial area per lipid and $A^\pm$ is the deformed area per lipid. The compression modulus of each monolayer does not need to be the same, hence K_a^+ represents the modulus for the upper leaflet and K_a^- is the modulus for the lower leaflet. As discussed later, for a protein of arbitrary shape with unmatched leaflet regions, a framework where the upper and lower leaflets can have different compression moduli becomes important when including *shell hardening* effects through spatially dependent moduli (1, 24) (see section S4.4).

Returning to Eq. S16, the compression energy can be rewritten in terms of the shape variables $u^\pm$ since the change in area $(A^\pm - A_0)$ is related to the vertical compression along the z-axis by means of the lipid volume constraint (25):

$$V = \chi V_0, \quad V_0 = h_0 A_0, \quad V = (h^+ - c)A^+ = -(h^- - c)A^-, \tag{S17}$$

where V_0 is the initial volume of the lipids, V is the volume of the lipids in the deformed configuration (assumed to be the same for the upper and lower leaflets) and $c(x, y)$ is the compression surface (11, 16, 26, 27) (Fig S5). The parameter $\chi \in [0, 1]$ is a phenomenological term describing the degree of volume conservation of the lipids before and after deformation. It is well known that the lipid volume is nearly incompressible (17, 25). For this reason, we have constrained our analysis in the main text to the incompressible case of $\chi \approx 1$, but note that our methods can accommodate lipid compressibility through the phenomenological variable χ. For a compressible lipid mix, there would be a new term appearing in the energy functional that can be treated as a line tension (linear on the deformation variable $u^\pm$). Having a line tension term in the energy functional can be easily accounted for using a change of variables (28, 29), resulting in no change to the form of the equilibrium equations. Using Eq. S17, the energetic penalty for compression in Eq. S16 can approximated up to quadratic order on the shape variables to be:

$$E_C = \int_{\Omega^+} \frac{K_a^+}{2h_0^2}\left[u^+ - c\right]^2 d\Omega^+ + \int_{\Omega^-} \frac{K_a^-}{2h_0^2}\left[u^- - c\right]^2 d\Omega^-. \tag{S18}$$

S4.3.1. Bilayer compression: matched regions

When the upper and lower leaflets match ($\Omega^+ = \Omega^- = \Omega_M$) the energy in Eq. S18 reduces to:

$$E_C = \int_{\Omega_M} \frac{K_a^+}{2h_0^2}\left[u^+ - c\right]^2 + \frac{K_a^-}{2h_0^2}\left[u^- - c\right]^2 d\Omega_M. \tag{S19}$$

For the static case, the deformations associated with the compression surface $c(x, y)$ will equilibrate very fast, and consequently, we can minimize over $c(x, y)$ without loss of generality (26, 27). The solution yields:

$$c(x, y) = \frac{K_a^+ u^+ + K_a^- u^-}{K_a^+ + K_a^-}. \tag{S20}$$

Using Eq. S20, the bilayer compression energy of the bilayer can be rewritten as:

$$E_C = \int_{\Omega_M} \frac{K_{eff}}{2h_0^2}\left[u^+ - u^-\right]^2 dxdy, \quad K_{eff} = \frac{K_a^+ K_a^-}{(K_a^+ + K_a^-)}, \tag{S21}$$

where K_{eff} is analogous to the effective spring constant of two Hookean springs coupled in series. In the main text, we have labeled the compression surface in matched regions $c = c_M(x, y)$.

S4.3.2. Bilayer compression: unmatched regions

When the area of protein insertion in the upper and lower leaflets do not match there is a region in space Ω_1 where the shape variable u^+ is not defined and/or a region Ω_2 where the variable u^- is not defined. For such scenarios, we expect that the surface of compression $c(x, y)$ is a function of the geometry of the inserted protein, where the energy minimization with respect to $c(x, y)$ is subject to a spatial constraint. As an illustrative example, we consider the insertion of a conically shaped protein shown in Fig. S5. In the unmatched region Ω_1 in the lower leaflet, the compression energy is described by:

$$E_C^- = \int_{\Omega_1} \frac{2K_a^-}{L_0^2}\left[u^- - c(x, y)\right]^2 - \lambda\left(c(x, y) - c_1\right) dxdy, \tag{S22}$$

where λ is the conjugate Lagrange multiplier to the constraint in the compression surface $c(x, y)$. The function c_1 is unknown and probably the result of complex coupling between the geometry of the membrane protein and distortion of the lipids. Fig. S5 shows a mismatch region between upper and lower surfaces that is described by an angle α. For small values of $(\pi/2 - \alpha)$ (small mismatch region Ω_1), we expect that the bilayer midplane c_M (compression surface in the matched region Ω_M) is not to heavily distorted such that the compression surface $c_1(x, y)$ in Ω_1 can be approximated as:

$$c_1(x, y) = \frac{h_B^+ + h^-(x, y)}{2}, \tag{S23}$$

where $h_B^+ = u_B^+ + h_0$ is the set of boundary conditions between the upper leaflet and protein (Fig. S5). Although we have used a conically shaped protein for illustrative purposes, the approximation in Eq. S23 is valid for proteins of arbitrary shape as long as the mismatched regions are moderately small. Importantly, this approximation preserves continuity of the midplane function $c(x, y)$ over the entire space. We make the same approximation in the lower leaflet for $u^-(x, y)$ in the region Ω_2:

$$c_2(x, y) = \frac{h_B^- + h^+(x, y)}{2}, \tag{S24}$$

where $h_B^- = u_B^- - h_0$ is the set of boundary conditions between the lower leaflet and protein (figure not shown). Note the deflection values $h^+(x, y)$ and $h^-(x, y)$ can in general vary in space along the boundary of the protein. In that case the values of h_B^+ and h_B^- inside the regions Ω_1 and Ω_2 are calculated through an interpolation procedure. We emphasize that in our proposed elastic model h_B^+ and h_B^- are prescribed as fixed conditions used to compute the compression plane $c(x, y)$ on mismatched regions.

S4.4. Hardening effects near the protein

The decreased conformational freedom of lipids near the boundary of an inclusion leads to greater molecular packing and greater resistance to elastic deformations – an effect known as *hardening* (1, 24). Partenskii and Jordan (24) accounted for this effect by developing a membrane free energy model where the elastic moduli were higher at the boundary of the inclusion, but returned to bulk values away from the protein-membrane interface with a decay length $\lambda_D \sim 15$ Å (comparable to the length of a lipid molecule). In their model the protein was assumed to be a cylinder and the slope condition was allowed to relax by using *natural BCs* on the curvature (See S5 for details on boundary conditions). Their model could describe experiments carried out on gramicidin (30) by only modulating the compression modulus as:

$$K_a(x,y) = \left[1 + (\Theta - 1) \cdot \exp\left(-\frac{r - r_0}{\lambda_D}\right)\right] K_{a,B}, \quad \text{for} \quad r \geq r_0, \tag{S25}$$

where $K_{a,B}$ is the bulk compression modulus, $\Theta \sim 4.5$ is the fitted phenomenological hardening factor, r_0 is the protein radius, and r is the radial distance from the protein center. Hence, lipids located $r - r_0 > 15$ Å from the protein have bulk-like behavior. Recently Lee et al. (22) noted that this approach still fails to provide bilayer thickness values consistent with molecular dynamics. We presume that these differences are due to the simplified protein representation in the elastic model and not the theoretical methodology. Therefore, in the main text we have implemented the Kim et al. (1), Partenskii and Jordan (24) hardening effect in the context of specific protein geometry. In our model, the upper (+) and lower (−) leaflet compression moduli follow from Eq. S25:

$$K_a^{\pm}(x,y) = \left[1 + (\Theta^{\pm} - 1) \cdot \exp\left(-\frac{r - r_0^{\pm}}{\lambda_D}\right)\right] K_{a,m}, \quad \text{for} \quad r \geq r_0^{\pm}, \tag{S26}$$

where $K_{a,m}$ is the monolayer bulk compression modulus, which we assume is half of the bilayer value $K_{a,B}$. For non-cylindrical proteins, the quantity $r - r_0^{\pm}$ is computed by identifying the membrane-protein contact point, $r_0^{\pm}$, that lies along the radial line connecting r to the origin. In general, the hardening field will be different in the upper and lower leaflets due to differences in the protein geometry in both leaflets (as in Fig. S5) leading to $K_a^+(x,y) \neq K_a^-(x,y)$. Therefore, when studying the distortions induced by arbitrary shape proteins, the bilayer compression modulus including the effects of hardening is readily given by the effective modulus K_{eff} in expression Eq. S21. Throughout this work, we set $\Theta^{\pm} \sim 4.5$ based on the gramicidin analysis in Ref. (24); however, it is possible to compare our calculations to deformation profiles determined from all-atom simulations to arrive at appropriate hardening values.

S4.5. Gaussian curvature

The Gaussian curvature energy in the upper leaflet is given by (see Refs. (11, 31, 32)):

$$E_G = -\frac{K_G}{2} \int_{\Omega^+} \vec{\nabla} \cdot \left[\left(\vec{\nabla}\vec{n}\right)\vec{n} - \left(\vec{\nabla} \cdot \vec{n}\right)\vec{n}\right] dxdy, \tag{S27}$$

where K_G is the Gaussian bending modulus, $\vec{n} = \nabla h^+$ is the two dimensional surface normal (neglecting the z-component), and we have dropped much of the leaflet specific notation. There is a similar energy term corresponding to the lower leaflet. In the expression above, we have used the notation $\vec{\nabla}\vec{n} = n_{j,k}$ to represent a second order tensor containing the derivatives of the normal vector $\vec{n}$ and hence $\left(\vec{\nabla}\vec{n}\right)\vec{n} = \left(\vec{n} \cdot \vec{\nabla}\right)\vec{n} = n_{j,k}n_k$ is a vector. With the divergence theorem, we can recast the Gaussian bending energy on the boundary $\partial\Omega$ as:

$$E_G = -\frac{K_G}{2} \oint_{\partial\Omega} \left[\left(\vec{\nabla}\vec{n}\right)\vec{n} - \left(\vec{\nabla} \cdot \vec{n}\right)\vec{n}\right] \cdot (-\vec{r})\, dl, \tag{S28}$$

where we define $\vec{r}$ as the outer normal to the surface describing the boundary $\partial\Omega$ in the x-y plane. Next, we show that the Gaussian contribution only depends on the boundary condition $\vec{n} = \vec{n}_0 = \nabla \vec{h}_0$ on $\partial\Omega$ (31, 32). To do this, we first define the tangential surface gradient operator (see Ref. (31)):

$$\vec{\nabla}_T\vec{n} = \vec{\nabla}\vec{n} - \left(\vec{\nabla}\vec{n}\right)\vec{r} \otimes \vec{r}, \tag{S29}$$

which essentially removes any contribution of the tensor $\vec{\nabla}_T\vec{n}$ in the normal direction to the surface $\vec{r}$. Consequently, $\vec{\nabla}_T\vec{n}$ only depends on tangential derivatives, or in other words, only values of $\vec{n} = \vec{n}_0$ on $\partial\Omega$. Making use of $\vec{\nabla}_T\vec{n}$, we can rewrite Eq. S28 as:

$$\begin{aligned}\left[\left(\vec{\nabla}\vec{n}\right)\vec{n} - \left(\vec{\nabla}\cdot\vec{n}\right)\vec{n}\right]\cdot\vec{r} &= n_{i,j}n_j r_i - n_{i,i}n_j r_j \\ &= \left(n_{i,j} - n_{i,k}r_k r_j\right)n_j r_i - \left(n_{i,i} - n_{i,k}r_k r_i\right)n_j r_j \\ &= \left[\left(\vec{\nabla}_T\vec{n}\right)\vec{n} - \mathrm{tr}\left(\vec{\nabla}_T\vec{n}\right)\vec{n}\right]\cdot\vec{r}.\end{aligned} \tag{S30}$$

From Eq. S30, we see that the Gaussian contribution Eq. S28 is only a function of normals $\vec{n}_0$ on the boundary. Consequently, if $\vec{n}_0$ is fixed as part of the boundary conditions, then there is no variation of the Gaussian energy E_G with respect to $\vec{n}$ at the boundary ($\delta(E_G)/\delta\vec{n} = 0$) and there is no contribution of the Gaussian component to the minimization equations. Thus, Eq. S28 does not influence the minimum energy configuration, but it must be included to determine the total energy of the system.

S4.5.1. Gaussian bending modulus K_G

Let c_1 and c_2 be the two principal curvatures such that mean curvature is $2H = c_1 + c_2$ and the Gaussian curvature is $K = c_1 \cdot c_2$. Then the energy density associated with changes in curvature is given by(9):

$$G = \frac{1}{2}K_c(H^2) + K_G(K) = [c_1, c_2]\cdot[\mathbf{A}]\cdot[c_1, c_2]^T, \quad \mathbf{A} = \begin{bmatrix} K_c & K_c + K_G \\ K_c + K_G & K_c \end{bmatrix}, \tag{S31}$$

where K_c is the bending modulus. For the free energy G to have a minimum, the matrix $\mathbf{A}$ must be positive definite, which requires $2K_c > -K_G > 0$. In the main text, we have used $K_G \sim -0.9K_c$ as recently measured from simulation (33).

S5. Boundary conditions at the membrane-protein contact curve

The total energy of the membrane-protein system (G^T) is given by the sum of the membrane elastic energy ($G^{(me)}$), the electrostatic energy ($G^{(e)}$), and the nonpolar energy $G^{(np)}$. For the elastic energy $G^{(me)}$, we assume that the only unknowns are the fields $u^+(x,y)$ and $u^-(x,y)$. The energy minimization is obtained using the variational formulation:

$$\delta G^{(me)}(u^+, u^-) = \delta G^{(me)}_{u^+} + \delta G^{(me)}_{u^-} = 0, \tag{S32}$$

where δG_{u^+} and δG_{u^-} represent the variation in energy resulting from variables u^+ and u^-, respectively. Eq. S32 yields the equilibrium shape equations of the membrane as well as a set of requirements (boundary conditions BCs) that the membrane deformation variables must satisfy at the boundary interface(34).

To see the role and physical significance of the BCs, we write the membrane's elastic energy functional $\delta G^{(me)}$ as the sum of the interior membrane surface contributions ($\delta G^{(me)}_\Omega$) and the contribution at the boundary edge ($\delta G^{(me)}_B$) (34):

$$\delta G^{(me)}\left(u^+, u^-\right) = \delta G^{(me)}_\Omega\left(u^+, u^-\right) + \delta G^{(me)}_B\left(u^+, u^-\right). \tag{S33}$$

Under the assumption that no external forces are acting over the interior surface of the membrane and that the only perturbations are due to the inclusion on the internal edge-boundaries, then the first term $\delta G^{(me)}_\Omega$ over the interior surface yields the Euler-Lagrange equations presented in the main text:

$$\nabla^4 u^+ - \nabla^2 J_0^+ - \gamma\nabla^2 u^+ + \beta\left(u^+ - u^-\right) = 0, \quad \text{in } \Omega_M, \tag{S34}$$

$$\nabla^4 u^- + \nabla^2 J_0^- - \gamma\nabla^2 u^- + \beta\left(u^- - u^+\right) = 0, \quad \text{in } \Omega_M, \tag{S35}$$

$$\nabla^4 u^- + \nabla^2 J_0^- - \gamma\nabla^2 u^- + \frac{\beta}{2}\left(u^- - u_B^+\right) = 0, \quad \text{in } \Omega_1, \tag{S36}$$

$$\nabla^4 u^+ - \nabla^2 J_0^+ - \gamma\nabla^2 u^+ + \frac{\beta}{2}\left(u^+ - u_B^-\right) = 0, \quad \text{in } \Omega_2, \tag{S37}$$

The second term $\delta G_B^{(me)}$ in Eq. S33 must account for the external shearing force $p_{ext}^{\pm}$ and mechanical moments $m_{ext}^{\pm}$ imposed by the inclusion at the edges (interior boundary) of the upper and lower leaflets, respectively. The latter yields the following set of allowable BCs (24):

$$\delta u^+ \left[p^+(u^+, u^-) - p_{ext}^+\right] + \delta\left(\nabla u^+ \cdot \vec{r}_2\right)\left[m^+(u^+, u^-) - m_{ext}^+\right] = 0 \quad \text{at the upper leaflet boundary,} \tag{S38}$$

$$\delta u^- \left[p^-(u^+, u^-) - p_{ext}^-\right] + \delta\left(\nabla u^- \cdot \vec{r}_1\right)\left[m^-(u^+, u^-) - m_{ext}^-\right] = 0 \quad \text{at the lower leaflet boundary,} \tag{S39}$$

where $\vec{r}_1$ is the unit vector pointing perpendicular to the curve described by the lower leaflet-protein interface and $\vec{r}_2$ is the unit vector pointing perpendicular to the curve described by the upper leaflet-protein interface (see Fig. 1 B in the main text). The variable $p^{\pm}$ represents the internal forces and $m^{\pm}$ are the internal moments generated at the interface by the stressed upper and lower leaflets.

From Eq. S38 and Eq. S39, we see that there there are several different BCs that satisfy the physical situation. The first, and most intuitive situation, is *fixed BCs*, where $u^{\pm}$ and $\vec{\nabla} u^{\pm}$ are predetermined at the boundaries. In this case, variations on the deformation variables at the boundary are zero ($\delta u^{\pm} = \delta \nabla u^{\pm} = 0$) and Eq. S38 - Eq. S39 are immediately satisfied. For the protein induced membrane distortion problem, we have following set of *fixed* conditions (See Refs. (24)):

$$\begin{aligned} &u^{\pm} = 0, \quad \vec{\nabla} u^{\pm} = 0 && \text{far away from inclusion, and} \\ &u^{\pm} = u_B^{\pm}, \quad \vec{\nabla} u^- \cdot \vec{r}_1 = S^-, \quad \vec{\nabla} u^+ \cdot \vec{r}_2 = S^+ && \text{at the protein-monolayer interface,} \end{aligned} \tag{S40}$$

where $S^{\pm}$ reflects the monolayer slope, or contact angle, at the point of contact with the protein. The fixed conditions *far away from the inclusion* in Eq. S40 are commonly used in the literature since it is expected that the protein induced membrane deformations should decay to bulk values; however, there is more disagreement about the appropriate BCs *at the protein-monolayer interface* in Eq. S40 (22). Earlier work found that setting the slopes equal to zero at the protein-membrane interface yielded compatible energetics with experiments carried out on gramicidin (24, 36, 37). Yet there is no formal justification for the zero slope condition, and more recent comparison with MD simulations suggests that the zero slope boundary condition fails to properly describe membrane deformations near the protein (22).

A second set of BCs compatible with Eq. S38 and Eq. S39 arise from the *physical* constraints of forces and torques at the membrane-protein interface (24):

$$p^+(u^+, u^-) = p_{ext}^+ \quad \text{and} \quad m^+(u^+, u^-) = m_{ext}^+ \quad \text{at the upper leaflet boundary,} \tag{S41}$$

$$p^-(u^+, u^-) = p_{ext}^- \quad \text{and} \quad m^-(u^+, u^-) = m_{ext}^- \quad \text{at the lower leaflet boundary.} \tag{S42}$$

It is not possible to know the analytic form of the constraints $p_{ext}^{\pm}$ and $m_{ext}^{\pm}$, thus precluding an easy implementation of these conditions. However, a special situations, referred to as *natural BCs*, arises when $u^{\pm}$ and/or $S^{\pm}$ are allowed to freely and independently adjust to the effects of the inclusion (22, 24). When $u^{\pm}$ is free to adjust, it implies no external forces are being applied ($p^{\pm} = 0$), while freely adjusting slopes ($S^{\pm}$) imply no externally applied moments ($m^{\pm} = 0$) (24). For instance, instead of fixing the value of $S^{\pm}$ at the boundary, many authors have used the alternative natural BCs of prescribing the *curvature* ($\nabla^2 u^{\pm} = 0$). For the case of gramicidin, it was determined that natural BCs on the curvature poorly correlated with experimental energies (22). Moreover, a formal mathematical derivation shows that the spontaneous J_0 and Gaussian modulus K_G should directly influence the curvature boundary condition (38). Both of these quantities are usually neglected in continuum elastic models that use the natural boundary condition on curvatures (22, 38). This could potentially contribute to the discrepancies reported between continuum elastic predictions and simulation/experiment.

S5.1. What are the correct boundary conditions for real proteins?

The unknown functional form of the forces $p_{ext}^{\pm}$ and torques $m_{ext}^{\pm}$ at the boundary precludes the use of a purely elastic continuum model for the membrane. Instead we use a hybrid continuum-atomistic model that couples the membrane deformation energy ($G^{(me)}$), non-polar energy ($G^{(np)}$) and electrostatic energy ($G^{(e)}$). The set of boundary conditions of the elastic model that minimizes the total energy of the system (G^T) is the key coupling element between the three explicit energies appearing in our hybrid approach. In the main text, we describe the optimization procedure used to minimize the energy by optimally choosing BCs, and these optimized displacement values at the protein-membrane boundary ($u_B^{\pm}$) are shown in Fig. 3 of the main text.

For completeness, the optimized slope boundary conditions ($S^{\pm}$) together with the slopes extracted from MD are shown in Fig. S6. The MD slope data is rather noisy due to the highly fluctuating nature of the gramicidin protein (center of mass translations, rotations, off axis tilting, and rotamer flipping), but our continuum slope predictions are in good agreement with the *average* values from MD. Convergence of the search over the boundary conditions depends on the protein's geometry and size, but generally it requires 500 to 1500 iterations to achieve an absolute convergence in the energy of 0.5 kcal/mol. Typical optimization times are about 2 to 7 hours on a desktop computer using a single core. As shown in Fig. S6, our optimized slopes are slightly positive and not zero as suggested by previous authors (13, 36, 37). Our solutions show evidence that at the protein-membrane interface, the slopes adapt in order to reduce the elastic penalty. This result agrees with the expected physical behavior for an elastic slab that is compressed. The hydrophobic region of gramicidin is slightly smaller than the hydrophobic thickness of the membrane (POPC), and in order to reduce the compression penalty near the protein the membrane returns to its undeformed shape more quickly resulting in non-zero slope. Having a positive slope will have a favorable effect to reduce compression at the expense of introducing curvature into the system. Including lipid hardening effects near the protein tends to increase the degree of the slope since the compression penalty increases. Despite our finding of a non-zero slope, the values reported here are smaller than the values reported previously (24) when using using lipid hardening in a membrane elastic model together with natural boundary conditions (free slope).

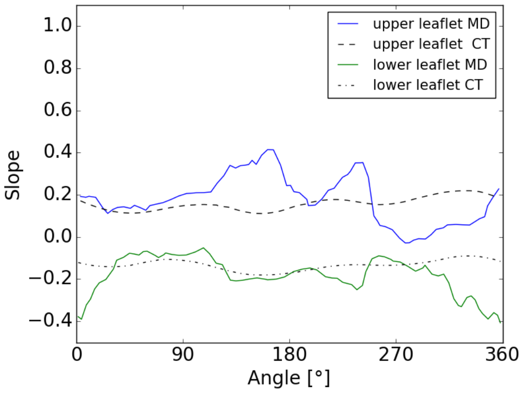

Figure S6: Predicted slopes at the protein-membrane boundary obtained from continuum calculations. The dotted line represents the optimal slope at the upper leaflet, and the dashed line corresponds to the slope values at the lower leaflet. The x-axis is the angular parameterization of the displacement along the membrane-protein boundary.

S6. Convergence of the continuum elastic energy.

We tested the convergence of our numeric solver for three different cases: an idealized cylindrical inclusion with $r_0 = 15$ Å, a configuration of gramicidin A examined in the main text, and the configuration of nhTMEM16 examined in our previous work (10). Each case has its own advantage. The cylinder has an analytic solution that we used to assess the absolute convergence of our method, while the later two cases are real proteins. Gramicidin is small and largely cylindrical, while nhTMEM16 is a large dimer with 20 transmembrane helices total (10). For the cylinder and gramicidin, solutions were calculated on a 100 Å by 100 Å grid, but nhTMEM16 is much larger, it was calculated on a 200 Å by 200 Å grid (10). For each boundary, we applied symmetric displacement boundary conditions: $u_B^{\pm} = \mp 1.5 \pm 1.5 \cdot \mathrm{Sin}(2t) \mp 1.5 \cdot \mathrm{Cos}(t)$. For the cylinder, a slope of zero was applied with no Partenskii-Jordan hardening near the protein, while the other two systems employed a hardening factor of 4.27 and a slope factor of -0.04. The error on the membrane displacement field was evaluated using the L^{∞}-norm, while the relative error was used to assess convergence of the total membrane energy (G^T). Analytic solutions do not exists for the gramicidin and nhTMEM16 cases, so the errors were calculated relative to the solution obtained at the highest grid density. In all cases, the greatest error over the entire displacement field is less than 0.7 Å when the grid spacing is less than 1.5 Å, which is greater than 64 grid points for A and B and greater than 128 grid points for C (Fig. S7). For the cylindrical inclusion, the error in the L^∞-norm asymptotically approaches 0.065 Å rather than 0 Å. The element corresponding to this maximum error is located on the outer boundary at 50 Å, where we assumed that the displacement field returned to zero in the numeric calculation, but we assume boundaries at infinity in the analytic solution. Thus, the true error in the numeric solver is even smaller than what is presented, due to inconsistencies between our numeric calculation and our analytic reference. The relative energies have converged to approximately 5 % in all cases when the grid spacing is 1 Å (Fig. S7 D-F). For all calculations in the main text, we use a grid spacing of 1 Å.

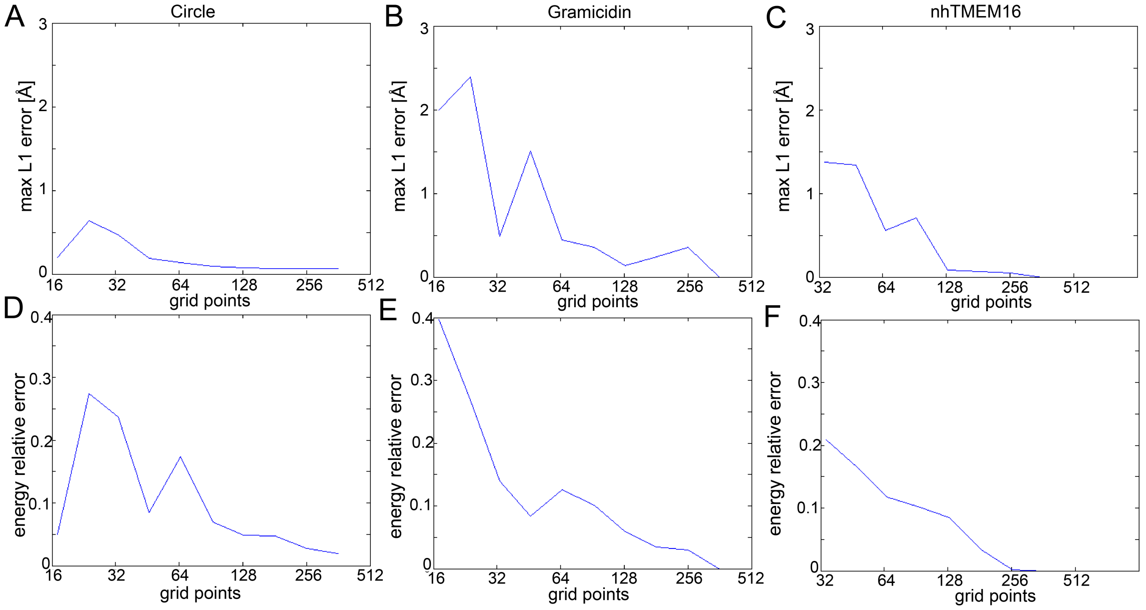

Figure S7: Convergence of membrane distortions on boundaries of different size and complexity. (A-C) L^∞-norm of the membrane shape variable for a cylinder of radius 15 Å, gramicidin, and nhTMEM16, respectively. The error is $E^\infty = \max\{u^{\text{numeric}}_{i,j} - u^{\text{analytic}}_{i,j}\}$ for the cylinder and $E^\infty = \max\{u^{\text{numeric}}_{i,j} - u^{\text{numeric max refinement}}_{i,j}\}$ for the two real proteins, and the indices i, j correspond to all elements in the xy-plane. Note that this error is identical to the maximum component of the L^1-norm as indicated in the figure label. (D-F) Relative error in the elastic energy for the cylinder, gramicidin, and nhTMEM16, respectively. The total energy for each test case was 8.8, 17.9, and 31.5 kcal/mol, respectively, where the last two values were determined from the numeric solution at the highest grid density and the former was determined analytically.

S7. Membrane height profiles from hybrid continuum-atomistic model.

Finally, we wanted to show the full 2D membrane profile predicted from our hybrid-continuum atomistic model (Fig. S8) using the self-consistently optimized membrane boundary displacements (shown in Fig. 4 of the main text) and slopes (Fig. S6). At the outer edges of the solution domain, we have imposed far field boundary conditions ($u^\pm = \nabla u^\pm = 0$). The corresponding membrane shape is quite similar in nature to the profiles from MD shown in Fig. 2A,B (main text); however, they are not identical for several important reasons. First, the MD simulations impose periodic boundaries and the continuum calculation in (Fig. S8) do not. Second, the profiles from the MD simulations are averaged over the entire simulation trajectory, while the continuum boundary conditions were taken from a small subset of protein configurations around the most populated orientation. As discussed throughout the manuscript, it is not advisable to closely compare deformation profiles of averaged membranes with static snapshots.

Supporting References

[1] T Kim, K Lee, P Morris, R W Pastor, O S Andersen, and W Im. Influence of Hydrophobic Mismatch on Structures and Dynamics of Gramicidin A and Lipid Bilayers. *Biophys. J.*, 102(7):1551–1560, 2012.

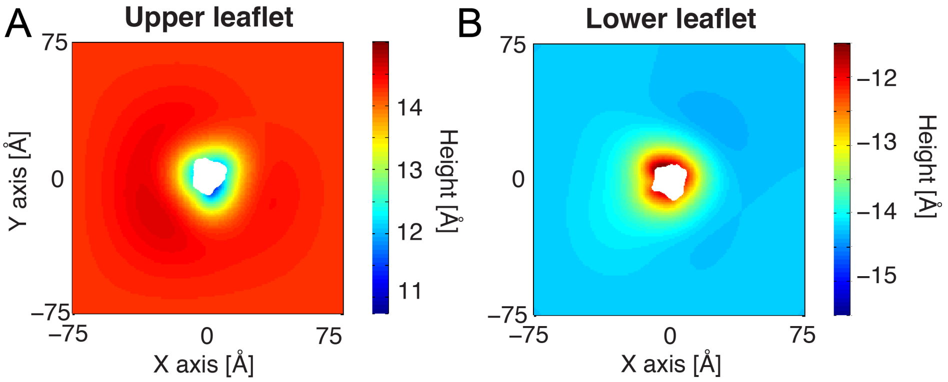

Figure S8: Gramicidin induced membrane deformations in the upper leaflet (A) and lower leaflet (B) calculated using our hybrid-continuum atomistic model. The boundary conditions at the protein-membrane interface are determined by a self-consistent optimization of our hybrid model. At the outer edges of the box we have imposed far field boundary conditions for the membrane deflections $u^{\pm} = \nabla u^{\pm} = 0$.

[2] KA Sharp and B Honig. Electrostatic interactions in macromolecules: Theory and applications. *Annual Review of Biophysics and Biophysical Chemistry*, 19(1):301–332, 1990. doi: 10.1146/annurev.bb.19.060190.001505.

[3] Nathan A Baker, David Sept, Simpson Joseph, Michael J Holst, and J Andrew McCammon. Electrostatics of nanosystems: Application to microtubules and the ribosome. *Proceedings of the National Academy of Sciences*, 98(18):10037–10041, 2001.

[4] K M Callenberg. *Membrane bending is critical for assessing the thermodynamic stability of proteins in the membrane.* PhD thesis, University of Pittsburgh, 2013.

[5] F V Marcoline, N Bethel, C J Guerriero, J L Brodsky, and M Grabe. Membrane protein properties revealed through data-rich electrostatics calculations. *Structure*, 23(8):1526–1537, 2015.

[6] N R Latorraca, K M Callenberg, J P Boyle, and M Grabe. Continuum approaches to understanding ion and peptide interactions with the membrane. *The Journal of Membrane Biology*, 247(5):395–408, 2014. ISSN 0022-2631. doi: 10.1007/s00232-014-9646-z.

[7] Michel F Sanner, Arthur J Olson, and Jean-Claude Spehner. Reduced surface: An efficient way to compute molecular surfaces. *Biopolymers*, 38(3):305–320, 1996.

[8] D Sitkoff, N Ben-Tal, and B Honig. Calculation of alkane to water solvation free energies using continuum solvent models. *The Journal of Physical Chemistry*, 100(7):2744–2752, 1996. doi: 10.1021/jp952986i.

[9] M Deserno. Fluid lipid membranes: From differential geometry to curvature stresses. *Chemistry and Physics of Lipids*, 185(0):11 – 45, 2015. ISSN 0009-3084. doi: http://dx.doi.org/10.1016/j.chemphyslip.2014.05.001.

[10] D Argudo, N P Bethel, F V Marcoline, and M Grabe. Continuum descriptions of membranes and their interaction with proteins: Towards chemically accurate models. *Biochimica et Biophysica Acta (BBA) - Biomembranes*, 1858:1619 – 1634, Jul 2016. ISSN 0005-2736. doi: http://dx.doi.org/10.1016/j.bbamem.2016.02.003.

[11] Max C Watson, Evgeni S Penev, Paul M Welch, and Frank L H Brown. Thermal fluctuations in shape, thickness, and molecular orientation in lipid bilayers. *J. Chem. Phys.*, 135(24):244701, 2011. doi: http://dx.doi.org/10.1063/1.3660673.

[12] J.-B. Fournier. Microscopic membrane elasticity and interactions among membrane inclusions: interplay between the shape, dilation, tilt and tilt-difference modes. *The European Physical Journal B - Condensed Matter and Complex Systems*, 11(2):261–272, 1999. ISSN 1434-6028. doi: 10.1007/BF03219168.

[13] H W Huang. Deformation free energy of bilayer membrane and its effect on gramicidin channel lifetime. *Biophys. J.*, 50(6):1061–1070, 1986.

[14] F Schmid. Are stress-free membranes really "tensionless"? *EPL*, 95(2):28008–, 2011.

[15] H Diamant. Model-free thermodynamics of fluid vesicles. *Phys. Rev. E.*, 84:061123–, 2011.

[16] Max C Watson, Alex Morriss-Andrews, Paul M Welch, and Frank L H Brown. Thermal fluctuations in shape, thickness, and molecular orientation in lipid bilayers. II. Finite surface tensions. *J. Chem. Phys.*, 139(8):084706, 2013. doi: http://dx.doi.org/10.1063/1.4818530.

[17] A Samuel Safran. *Statistical Thermodynamics of Surfaces, Interfaces, and Membranes*. Westview Press, Boulder, Colorado, 2003. Frontiers in Physics.

[18] A F Bitbol, D Constantin, and J.-B. Fournier. Bilayer Elasticity at the Nanoscale: The Need for New Terms. *PLos ONE.*, 7(11):–, 2012. doi: 10.1371/journal.pone.0048306.

[19] S Choe, K A Hecht, and M Grabe. A continuum method for determining membrane protein insertion energies and the problem of charged residues. *J. Gen. Physiol.*, 131(6):563–573, 2008.

[20] Keith M Callenberg, Om P Choudhary, Gabriel L de Forest, David W Gohara, Nathan A Baker, and Michael Grabe. Apbsmem: A graphical interface for electrostatic calculations at the membrane. *PLoS ONE*, 5(9):e12722–, 09 2010. doi: 10.1371/journal.pone.0012722.

[21] K M Callenberg, N R Latorraca, and M Grabe. Membrane bending is critical for the stability of voltage sensor segments in the membrane. *The Journal of General Physiology*, 140(1):55–68, 2012. doi: 10.1085/jgp.201110766.

[22] K Lee, R W Pastor, O S Andersen, and W Im. Assessing smectic liquid-crystal continuum models for elastic bilayer deformations. *Chemistry and Physics of Lipids*, 169(0):19 – 26, 2013. doi: http://dx.doi.org/10.1016/j.chemphyslip.2013.01.005. Computational approaches to

understanding lipid-protein interactions.

[23] D Boal. *Mechanics of the Cell*. Cambridge University Press, Cambridge, 2nd edition, 2012.

[24] M B Partenskii and P C Jordan. Membrane deformation and the elastic energy of insertion: Perturbation of membrane elastic constants due to peptide insertion. *The Journal of Chemical Physics*, 117(23):10768–10776, 2002. doi: http://dx.doi.org/10.1063/1.1519840.

[25] Aranda-Espinoza, H and Berman, A and Dan, N and Pincus, P and Safran, S. Interaction between inclusions embedded in membranes. *Biophys. J.*, 71(2):648–656, 1996.

[26] Miha Fošnarič, Ale š Iglič, and Sylvio May. Influence of rigid inclusions on the bending elasticity of a lipid membrane. *Phys. Rev. E*, 74(5): 051503–, 2006. doi: 10.1103/PhysRevE.74.051503.

[27] R J Bingham, P D Olmsted, and S W Smye. Undulation instability in a bilayer lipid membrane due to electric field interaction with lipid dipoles. *Phys. Rev. E*, 81(5):051909–, 2010. doi: 10.1103/PhysRevE.81.051909.

[28] A C Haselwandter and R Phillips. Connection between oligomeric state and gating characteristics of mechanosensitive ion channels. *PLoS Comput Biol.*, 9(5):1–13, 2013.

[29] C A Haselwandter and R Phillips. Directional interactions and cooperativity between mechanosensitive membrane proteins. *EPL*, 101(6): 68002–, 2013. doi: 10.1209/0295-5075/101/68002.

[30] M Goulian, O M Mesquita, D K Fygenson, C Nielsen, O S Andersen, and A Libchaber. Gramicidin channel kinetics under tension. *Biophys. J.*, 74(1):328–337, 1998.

[31] Robert Hardt, David Kinderlehrer, and Fang-Hua Lin. Existence and partial regularity of static liquid crystal configurations. *Communications in Mathematical Physics*, 105(4):547–570, 1986.

[32] I W Stewart. *The static and dynamic continuum theory of liquid crystals*. Taylor and Francis, London, UK, 2004.

[33] M Hu, H de Jong, S Marrink, and M Deserno. Gaussian curvature elasticity determined from global shape transformations and local stress distributions: a comparative study using the MARTINI model. *Faraday Discuss.*, 161:365–382, 2013.

[34] O Bolza. *Lectures on the Calculus of Variations*. Dover Publications, New York, 1961.

[36] Nielsen, C and Goulian, M and Andersen, O S. Energetics of inclusion-induced bilayer deformations. *Biophys. J.*, 74(4):1966–83, 1998.

[37] Nielsen, C and Ansersen, O S. Inclusion-induced bilayer deformations: effects of monolayer equilibrium curvature. *Biophys. J.*, 79(5): 2583–2604, 2000.

[38] G Brannigan and F L H Brown. Contributions of Gaussian Curvature and Nonconstant Lipid Volume to Protein Deformation of Lipid Bilayers. *Biophys. J.*, 92(8):864–876, 2007.